

Quantifying bedrock-fracture patterns within the shallow subsurface: Implications for rock mass strength, bedrock landslides, and erodibility

Brian A. Clarke^{1,2} and Douglas W. Burbank¹

Received 9 February 2011; revised 24 June 2011; accepted 13 July 2011; published 22 October 2011.

[1] The role of bedrock fractures and rock mass strength is often considered a primary influence on the efficiency of surface processes and the morphology of landscapes. Quantifying bedrock characteristics at hillslope scales, however, has proven difficult. Here, we present a new field-based method for quantifying the depth and apparent density of bedrock fractures within the shallow subsurface based on seismic refraction surveys. We examine variations in subsurface fracture patterns in both Fiordland and the Southern Alps of New Zealand to better constrain the influence of bedrock properties in governing rates and patterns of landslides, as well as the morphology of threshold landscapes. We argue that intense tectonic deformation produces uniform bedrock fracturing with depth, whereas geomorphic processes produce strong fracture gradients focused within the shallow subsurface. Additionally, we argue that hillslope strength and stability are functions of both the intact rock strength and the density of bedrock fractures, such that for a given intact rock strength, a threshold fracture-density exists that delineates between stable and unstable rock masses. In the Southern Alps, tectonic forces have pervasively fractured intrinsically weak rock to the verge of instability, such that the entire rock mass is susceptible to failure and landslides can potentially extend to great depths. Conversely, in Fiordland, tectonic fracturing of the strong intact rock has produced fracture densities less than the regional stability threshold. Therefore, bedrock failure in Fiordland generally occurs only after geomorphic fracturing has further reduced the rock mass strength. This dependence on geomorphic fracturing limits the depths of bedrock landslides to within this geomorphically weakened zone.

Citation: Clarke, B. A., and D. W. Burbank (2011), Quantifying bedrock-fracture patterns within the shallow subsurface: Implications for rock mass strength, bedrock landslides, and erodibility, *J. Geophys. Res.*, 116, F04009, doi:10.1029/2011JF001987.

1. Introduction

[2] Hillslope-scale rock strength plays a fundamental role in landscape evolution by influencing surface morphology and resisting erosive processes. Bedrock strength at hillslope scales limits topographic relief [Schmidt and Montgomery, 1995], sets thresholds for the maximum angle of slope stability [Selby, 1992; Burbank *et al.*, 1996; Montgomery, 2001], and influences bedrock erodibility [Gilbert, 1877; Carson and Kirkby, 1972; Stock and Montgomery, 1999; Duvall *et al.*, 2004; Molnar *et al.*, 2007]. The strength of intact rock, like other solid materials, is the product of cohesive and frictional forces [Coulomb, 1776; Hoek and Bray, 1997; Jaeger *et al.*, 2007]. Fractures or any structural discontinuity reduce cohesion and internal friction by

severing bonds between particles and creating discrete failure surfaces [Terzaghi, 1962; Carson and Kirkby, 1972]. Dense, intersecting fractures have the potential to completely disintegrate rock fragments, which in turn minimizes cohesion at decimeter- to meter-scales and reduces internal friction to the friction between disjointed fragments, as opposed to the friction between mineral grains within the intact rock. In general, rock mass strength decreases over increasing spatial scales due to the increased abundance of fractures and discontinuities. Hillslope-scale rock mass strength incorporates the intact rock strength, the degree of weathering, and the intensity and characteristics of bedrock fractures [Deere, 1964; Selby, 1980, 1992; Schmidt and Montgomery, 1995; Hoek and Brown, 1997; Jaeger *et al.*, 2007]. In all mountainous terrain, it is the broad-scale strength of the underlying rock mass that opposes gravity to support relief and resists erosional processes.

[3] In rapidly eroding, threshold landscapes, rates of erosion outpace rates of soil production, resulting in bedrock-dominated hillslopes. In these threshold regions, the mechanical strength of the rock mass is posited to limit

¹Department of Earth Science, University of California, Santa Barbara, California, USA.

²Institute for Earth and Environmental Science, Universität Potsdam, Potsdam, Germany.

the maximum angle of hillslope stability, such that modal hillslope angles are directly related to hillslope-scale rock mass strength [Selby, 1992; Schmidt and Montgomery, 1995; Burbank et al., 1996; Montgomery, 2001; Korup, 2008; Lin et al., 2008; Clarke and Burbank, 2010]. Hillslopes that are steepened beyond threshold angles, by rock uplift and valley incision, are inherently unstable and prone to failure by bedrock landslides, which subsequently reduces these over-steepened slopes toward threshold angles of stability [Burbank et al., 1996; Montgomery, 2001; Lin et al., 2008; Clarke and Burbank, 2010]. In addition to influencing hillslope stability, fractures that disintegrate rock fragments or severely weaken the rock mass also produce near-surface material that is far more readily removed by erosive processes than is pristine, intact rock [Gilbert, 1877; Carson and Kirkby, 1972; Molnar et al., 2007].

[4] Quantifying rock mass strength, however, is notoriously difficult. Although metrics of mechanical rock strength have been well defined in small-scale laboratory studies [Brady and Brown, 2006; Hoek and Bray, 1997; Jaeger et al., 2007], extrapolation to hillslope scales is not straightforward due to the increasing presence of fractures, discontinuities, and bedrock heterogeneity. Even though the same principles apply at all scales, the inability to make strength measurements at large scales relevant to geomorphic processes has greatly limited understanding of how rock mass strength influences landscape form and surface processes.

[5] Numerous semiquantitative proxy classification schemes have been developed to assess rock mass strength at hillslope scales, e.g., the rock mass strength (RMS) classification, geologic strength index (GSI), or rock mass rating (RMR): [Selby, 1980, 1992; Bieniawski, 1989; Hoek and Brown, 1997]. Trends have been shown relating these proxy classification techniques to landscape form and process rates [Selby, 1980, 1992; Moon and Selby, 1983; Korup and Schlunegger, 2009; Moore et al., 2009]. Whereas these relationships provide further evidence that the strength of hillslope-scale rock mass is a fundamental control on geomorphology, they do not provide a quantitative, mechanistic linkage between rock strength, form, and process. These classification methods rely on qualitative assessment of bedrock characteristics and primarily evaluate surface attributes from exposed bedrock outcrops. Bedrock characteristics and strength, however, display wide spatial variability both horizontally across the landscape and vertically with depth. Moreover, the rock mass strength of the subsurface exerts a primary control on how hillslopes evolve in most landslide-dominated terrains. Unfortunately, the traditional, outcrop-based classifications of rock mass strength reveal little about key strength attributes at subsurface depths. Therefore, a depth-dependent assessment of bedrock resistance is needed both to illuminate the extent to which erosional efficiency can be modulated by the strength of the rock mass, as well as to constrain the evolution of that strength as material from the surface is removed and replaced by material from greater depths.

[6] Here we present a new technique that integrates field- and laboratory-based seismic surveys with numerical modeling of subsurface velocity structures in order to quantify depth-dependent patterns of bedrock fractures. We present a comparative analysis of the Southern Alps and Fiordland regions of New Zealand: ranges characterized by similar

climatic forcing, but stark contrasts in rock-uplift rates and underlying lithologies. Differences in valley cross-sectional profiles and the topographic imprint of bedrock landslides between these regions have been attributed to contrasts in rock-strength [Augustinus, 1992b, 1995; Korup, 2005, 2008]. Clarke and Burbank [2010] showed that hillslopes in both regions are maintained at equivalent threshold gradients, despite significant differences in rock types and the rates of bedrock landsliding. They used a simple seismic profile analysis to deduce that bedrock fractures in the near surface strongly influence threshold slope angles, whereas the depth of bedrock fracturing modulates landslide magnitude. We build upon this work by implementing more sophisticated subsurface modeling techniques that allow us to quantify depth-dependent variations in bedrock-fracture patterns and assess apparent volumetric fracture densities within the shallow subsurface. Based on these depth profiles, we show that fundamental differences exist in the pattern of bedrock fractures between the Southern Alps and Fiordland and that these differences influence the mechanical strength of hillslopes and the depths of bedrock landslides. This new approach provides a simple, easily applicable, and quantitative means to assess hillslope-scale mechanical properties. Moreover, this approach provides some of the first quantitative evidence relating the depth and density of bedrock fractures to the magnitude of deep-seated bedrock landslides.

2. Background and Study Area

[7] The Southern Alps and Fiordland, both located on the western coast of the South Island of New Zealand (Figure 1), have formed due to the ongoing, oblique convergence of the Pacific and Australian plates [DeMets et al., 1990]. The Southern Alps comprise material that is detached from the upper portion of the westward-subducting Pacific plate, is accreted onto the orogenic wedge of the Southern Alps, and is then thrust up to the surface along the steep, east-dipping Alpine fault [Koons, 1989, 1990; Beaumont et al., 1996]. The Southern Alps comprise low-grade metamorphic rocks (Figure 1b) ranging from the ubiquitous Torlesse group (greywacke and argillite) in the east to its aerially restricted, low- to medium-grade schist derivatives in the west [Mason, 1962]. In Fiordland, although rock mass is driven upward by the eastward subduction of the Australian plate, rock is not advected through the orogen as occurs in the Southern Alps [Sutherland et al., 2000; Malservisi et al., 2003]. Fiordland comprises igneous and high-grade metamorphic rocks with a cap of metasedimentary rock in the range's core [Bradshaw, 1990] (Figure 1b). Due to the close spatial proximity and generally similar topography of Fiordland and the Southern Alps, they experience similar precipitation patterns (Figure 1) and have undergone temporally and spatially similar glacial-interglacial transitions throughout the Quaternary [Griffiths and McSaveney, 1983; Suggate, 1990; National Institute of Water and Atmospheric Research, 2000]. Whereas the western flanks of both regions receive strikingly high annual precipitation (>8 m/yr in some areas), an orographic gradient sharply reduces precipitation from west to east (Figure 1a).

[8] Fiordland and the Southern Alps exhibit starkly different long-term rates of rock-uplift. In the Southern Alps,

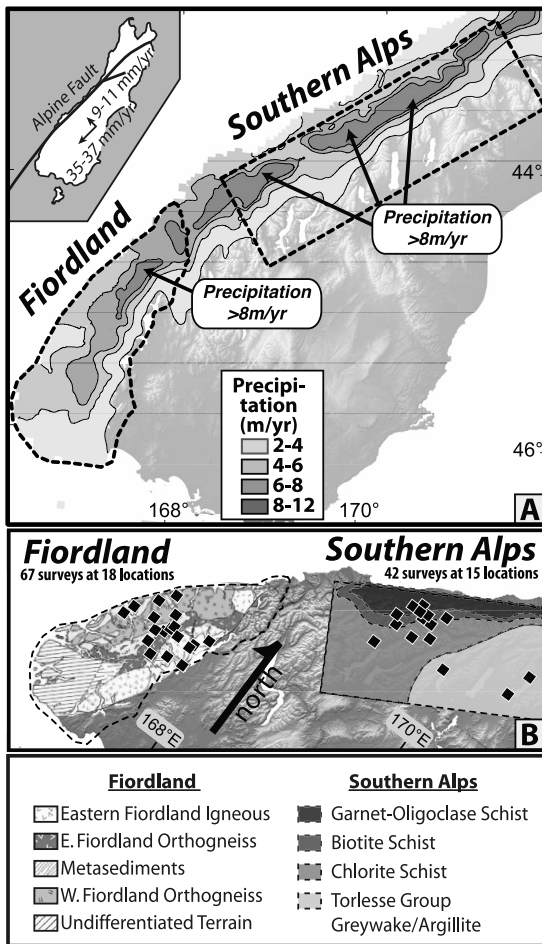


Figure 1. Location, precipitation, and geology of the Southern Alps and Fiordland, New Zealand. (a) Patterns of precipitation [National Institute of Water and Atmospheric Research, 2000] and locations of the two study regions (dashed lines). Inset shows plate motion relative to the Alpine Fault. (b) Locations of seismic survey sites and simplified geologic maps for Fiordland and the Southern Alps. Modified from Bradshaw [1990] and Beaumont et al. [1996].

rates attain 7–11 mm/yr on the rain-soaked West Coast and decrease sharply across the divide to the east [Kamp and Tippett, 1993; Tippett and Kamp, 1993; Herman and Braun, 2006; Herman et al., 2007, 2009]. Although less well-constrained, rock-uplift rates in Fiordland range between ~0.2 and ~1 mm/yr [House et al., 2002, 2005; Sutherland et al., 2009]: ~5 to 20 times slower than those of the Southern Alps. Despite these contrasts in uplift rates and rock type, both ranges are characterized by similar modal slopes of ~32° [Clarke and Burbank, 2010]. Additionally, landslide mapping on a time series of spatially overlapping aerial-photos reveals power law trends within the landslide magnitude-frequency distributions in each range (Figure 2). Integration of these data reveals short-term (10–100 yr) average erosion rates by bedrock landslides of 9 ± 4 mm/yr in the western Southern Alps [Hovius et al., 1997] and between 0.1 ± 0.05 and 0.3 ± 0.1 mm/yr in Fiordland [Clarke and Burbank, 2010]. Based on the slopes of the power law regressions (Figure 2), the largest landslides in

both ranges are interpreted to provide the dominant volumetric contribution to erosion [Hovius et al., 1997; Clarke and Burbank, 2010]. Comparisons of landslide magnitude-frequency distributions between the two regions, however, reveal order-of-magnitude differences in both the overall frequency of landsliding events and the size of the largest observed landslides (Figure 2). Landslides in Fiordland are considerably smaller and less frequent than in the Southern Alps. Estimates of landslide depths can be made by using scaling relationships between landslide area (Figure 2) and depth, where landslide depth is estimated as 0.05 ± 0.02 times the square-root of landslide area [Ohmori and Hirano, 1988; Ohmori, 1992; Hovius et al., 1997; Lavé and Burbank, 2004; Larsen et al., 2010]. In the Southern Alps, the largest observed landslides are predicted to have depths of ~50 m, whereas in Fiordland, maximum landslide depths are predicted to typically be ~15 m (Figure 2).

[9] Clarke and Burbank [2010] argued that the similarity in modal threshold slope angles (~32°) and the differences in estimated landslide depths could be attributed to differences in the patterns of bedrock fracturing that are revealed through curvature analysis of seismic time-distance profiles. They interpreted differences in curvature to result from depth-dependent differences in bedrock-fracture densities. Although this simple, curvature-based method depicts clear contrasts between Fiordland and the Southern Alps, here we implement more sophisticated seismic interpretation techniques to extract quantitative, depth-constrained information on subsurface velocity profiles and bedrock-fracture patterns, which in turn allows us to examine the relationship between bedrock fractures, hillslope-scale rock mass strength, and landslide distributions in these threshold landscapes.

3. Methods and Results

[10] We integrate measures of seismic p-wave (sound-wave) velocities from field surveys and laboratory samples

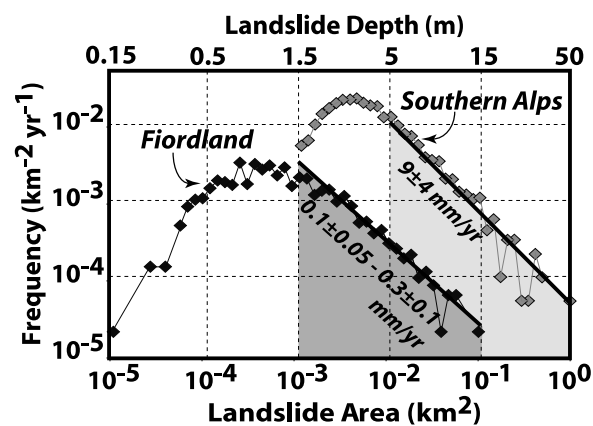


Figure 2. Landslide magnitude-frequency distributions for the western Southern Alps (gray rectangles) and Fiordland (black rectangles). Landslide area has been converted into estimates of landslide depth (see text for details). The shaded regions identify the portion of each distribution that is best characterized by a power law trend, which is then used to derive estimates for rates of landslide-driven erosion [Hovius et al., 1997; Clarke and Burbank, 2010].

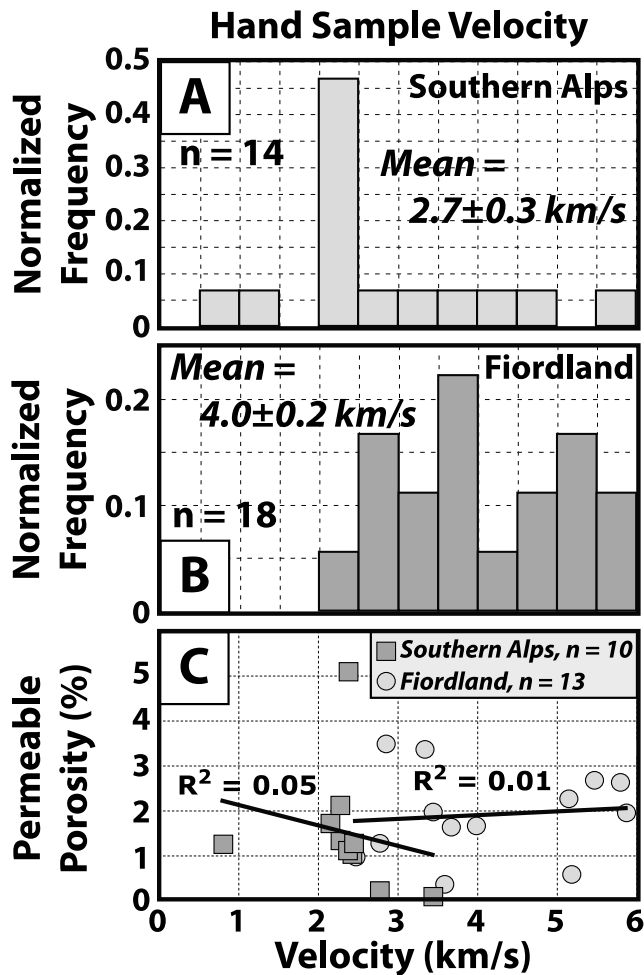


Figure 3. Laboratory measurements of hand samples. Distributions of sample p-wave velocity with standard errors for (a) the Southern Alps and (b) Fiordland. (c) Laboratory measurements reveal low permeably interconnected porosity in all samples and show no significant correlation between these low-porosity values and measured hand-sample velocity.

with two numerical models in order to assess bedrock fracturing in the shallow subsurface. The first model inverts seismic refraction field surveys to both establish hillslope-scale subsurface velocity profiles and identify depths where sharp velocity contrasts exist. The second model utilizes the velocity depth-profiles in conjunction with laboratory-based measurements of intact bedrock velocity to determine the apparent volumetric fracture density with depth that would reduce the intact bedrock velocity, such that it matches the modeled velocity profiles. By combining these two models, we are able to quantify depths, densities, and gradients of bedrock fractures within the shallow subsurface.

3.1. Field and Laboratory Velocity Measurements

[11] We conducted shallow seismic refraction surveys over a dense array of sites that span both the width of each range and every major rock unit across them (Figure 1b). All surveys were conducted along linear trends as directly as possible on bedrock surfaces and, where applicable, were oriented perpendicular to foliation planes or any obvious

fracture orientations. Surveys were primarily collected along ridges, with additional surveys in both regions collected from the middle and lower reaches of hillslopes adjacent to valley bottoms in locations where bedrock visibly cropped out along the survey line. Where soils or regolith were present, thicknesses were estimated to always be less than 0.5 m and were usually much less than 0.2 m (based on visibly projecting the exposed bedrock beneath the thin surface cover). Following standard seismic refraction survey methods [Mussett and Khan, 2000], we used a Geometrics Smartseis seismograph, 8–12 geophones depending on available space at the survey sites, and a sledgehammer and steel plate as the seismic source. Survey lengths ranged from 10 m to 60 m with a mean length of ~36 m. P-wave first-arrival times were measured at successive geophones with geophone spacing ranging from 1 m to 5 m. In a few cases, the p-wave first-arrival time at individual geophones could not be reliably determined due to external noise, such as wind, moving vegetation, or faulty connections. In such cases, first-arrival times for that geophone were not used in further analysis.

[12] We estimate the intact bedrock velocity based on laboratory measurements of hand samples collected from all but one field site. Samples were removed from intact bedrock and contained no obvious fractures. The p-wave velocity of each sample was measured in the laboratory using cylindrical rock cores 2.5 cm in diameter and 2.5 cm long that were drilled from the intact hand samples (see auxiliary material).¹ The average Fiordland laboratory sample velocity ($n = 18$) and standard error is 4.0 ± 0.2 km/s, whereas the average Southern Alps velocity ($n = 14$) is only 2.7 ± 0.3 km/s (Figures 3a and 3b). The 1.5-fold difference in intact velocity between the regions is not surprising given the strong contrast between the schists of the Southern Alps versus the igneous and metamorphic rocks of Fiordland (Figure 1b). Measures of porosity were made for a selection of hand samples from both regions by placing the rock cores into pressurized chambers and measuring the volume of gas that permeates into the core (Figure 3c). These porosity measurements, however, only account for the volume of pore-space that is permeably connected to the surface of the rock core. This permeable porosity is low in both regions, occupying only a few percent of the total sample volume, and appears uncorrelated with the laboratory velocity measurements (Figure 3c). We assume, therefore, that the p-wave velocities measured in these hand samples provide reasonable estimates for the velocity of intact bedrock at each survey site.

3.2. Subsurface Velocity Model

[13] Inversion of 2-D seismic refraction surveys has been widely used to identify subsurface velocity structures and bedrock characteristics [Palmer, 1981; Telford et al., 1990; Zelt and Smith, 1992; Hack, 2000; Forbriger, 2003a, 2003b, and references therein]. Our approach follows the standard inversion methods outlined in most introductory geophysics textbooks [e.g., Sheriff and Geldart, 1982; Mussett and Khan, 2000]. When first-arrival times of seismic-waves at successive geophone sensors are plotted as a function of

¹Auxiliary materials are available in the HTML. doi:10.1029/2011JF001987.

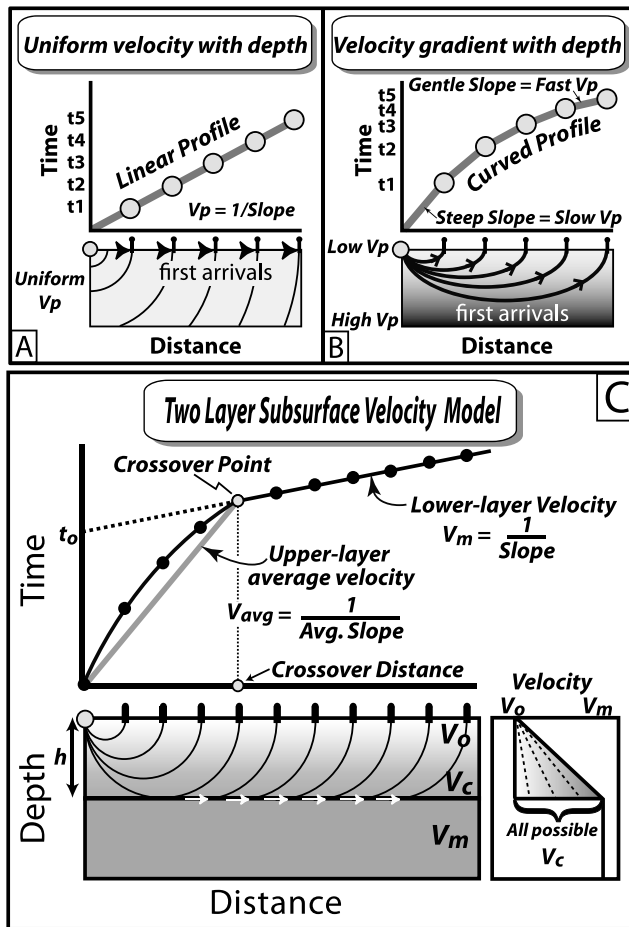


Figure 4. Schematic seismic survey profiles and time-distance curves. (a) Predicted time-distance data for bedrock with uniform p-wave velocity (V_p). Lower box depicts a vertical shallow-subsurface cross-section, where the thin, black curved lines represent seismic wave propagation. Black arrows denote the fastest raypath between the seismic source and each geophone. Upper plot shows the linear time-distance profile due to uniform seismic velocity. (b) Schematic seismic survey over bedrock with a velocity gradient, showing that deeper rocks are seismically faster. The first-arrival raypath from the source to each successive geophone extends to ever-greater depths and exploits faster velocities (curved lines with arrows), resulting in a curved time-distance profile. (c) Seismic velocity model geometry comprises an upper layer with a linearly increasing velocity gradient with depth and a lower layer with a uniform velocity. The velocity gradient in the upper layer produces the initial curve in the time-distance profile, whereas the uniform lower layer produces a linear time-distance trend in the later part of the profile. The “crossover point” marks the intersection of these two segments, which occurs at the “crossover distance” from the seismic source. The model determines the velocity parameters and subsurface geometry that produce the best match to the measured seismic surveys (see text for model details).

distance from the seismic source, the p-wave velocity can be calculated as the reciprocal of the instantaneous slope along the time-distance profile (Figure 4). Hence, a steep slope in time-distance space indicates a slow velocity, whereas

gentle slopes are indicative of fast velocities. Because subsurface seismic velocity is the result of meso-scale rock mass characteristics, the observed time-distance profiles provide an integrative measure of intact rock, bedrock fractures (water- or air-filled), any soil cover, and any other sources of velocity variability along the length or depth of the profile [Hudson, 1981; Palmer, 1981; Hack, 2000; Mussett and Khan, 2000].

[14] Seismic surveys over spatially homogeneous bedrock produce a straight line through successive arrivals in a time-distance plot (Figure 4a). In this scenario, seismic waves radiate in all directions away from the seismic source and travel at uniform velocities through the bedrock. Therefore, first-arrival times are produced by direct seismic-raypaths that travel along the profile surface (Figure 4a). Seismic surveys conducted over bedrock that is characterized by increasing velocity with depth, as would be expected in bedrock that is densely fractured at the surface but not at depth, produce time-distance plots with distinct negative curvature [Sheriff and Geldart, 1982; Hack, 2000; Forbriger 2003b] (Figure 4b). In this scenario, seismic waves that originate at the surface, but travel to greater depths, encounter faster velocity rock that causes the waves to refract, following Snell’s law, and bend back toward the surface (Figure 4b). Over increasing distances, the first-arrival waves will have traveled to greater depths and at faster velocities, thereby tracing arcuate pathways to each successive geophone (Figure 4b). To the extent that velocities continue to increase with depth, the time-distance curve will display an ever-decreasing slope, resulting in profiles with negative curvature (Figure 4b). Both the magnitude of curvature and the distance over which curvature persists in time-distance space are dependent on the subsurface velocity gradient [Sheriff and Geldart, 1982; Forbriger, 2003b]. A linear increase in velocity with depth results in semi-circular seismic-raypaths in the subsurface and constant curvature in the time-distance plot [Sheriff and Geldart, 1982] (Figure 4b). Although actual seismic refraction profiles can be far more complicated than these end-member scenarios, they can usually be subdivided into either linear or curved sections that correspond to subsurface regions characterized by either uniform or graduated velocity structures, respectively (Figure 4c).

[15] Initial assessment of our time-distance data reveals that our surveys can be broadly characterized as displaying either (1) an entirely linear profile (Figure 4a and Figure 5, profile iv), (2) a profile with constant curvature over the entire survey length (Figure 4b and Figure 5, profile ii), or (3) a profile composed of a curved initial section followed by a linear trend at greater distances from the seismic source (Figure 4c and Figure 5, profiles i and iii). For time-distance plots of all seismic surveys, see auxiliary material.

[16] To explore the velocity implications of our data more rigorously, we develop a seismic inversion model that systematically determines the subsurface velocity structure that best characterizes each of the field surveys. To account for both the curved and linear sections of the time-distance profiles, the model implements a two-layer geometry in which an upper layer with a velocity gradient sits directly above a lower layer of uniform velocity (Figure 4c). The subsurface velocity structure and upper-layer depth dictate the curvature of the time-distance profile and the extent to

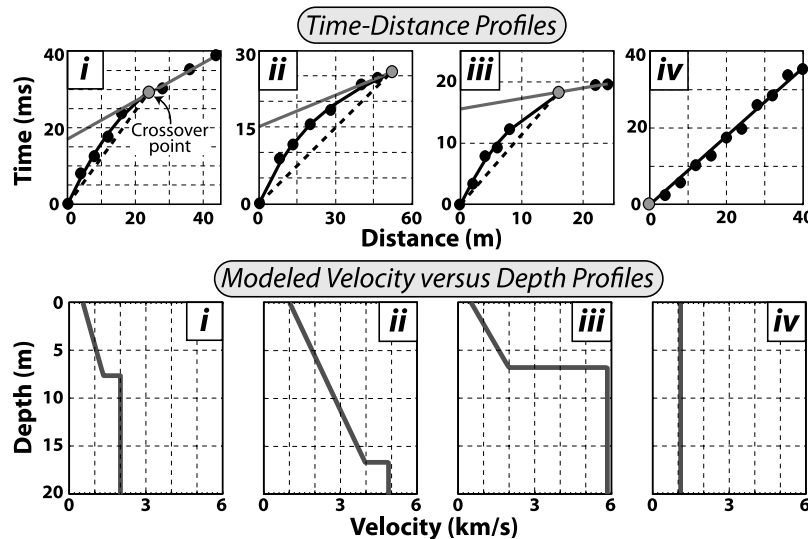


Figure 5. Examples of time-distance profiles and modeled velocity results. (top) First-arrival times as a function of distance along each survey profile (black dots) with the best fit crossover point indicated (gray dot) and the best fit model results for the upper layer (black line), average upper layer (dashed line), and lower layer (gray line). (bottom) Corresponding velocity versus depth profiles based on the time-distance data. Profiles i–iii display multilayer velocity profiles, whereas profile iv is best modeled as a single, uniform-velocity layer.

which the modeled profile is dominated by curved versus linear trends (Figure 4c). Even though the model implements a two-layer geometry, a single subsurface layer with uniform velocity can still be modeled by imposing an upper-layer depth of zero, which produces a linear time-distance profile (Figure 4a). Conversely, a profile with constant curvature over the full length of the survey can be modeled by imposing an upper-layer depth equal to or greater than the maximum penetrative depth of the seismic raypath that travels from the seismic source to the farthest geophone (Figure 4b). An iterative, parameter-search based approach is used to determine the subsurface geometry and velocity structure that best characterizes each of the field surveys.

[17] Because of the inevitable noise in the field data, we assume that if a linear fit to the entire time-distance profile can explain >95% of the variance ($r^2 > 0.95$), that no upper layer exists (the upper-layer depth equals zero), and the profile is considered to represent a single layer of uniform velocity. The velocity of this single layer is determined as the reciprocal of the slope of the best linear fit to the data. Conversely, whenever a linear fit to the entire profile produces an $r^2 \leq 0.95$, the two-layer model is implemented.

[18] The two-layer model assumes a linear velocity gradient in the upper layer, a uniform velocity layer at depth, and a thin boundary between these layers that commonly defines an offset in velocity between the two layers (Figure 4c). This model predicts a curved initial profile, corresponding to the velocity gradient in the upper layer, followed by a linear portion ascribed to the uniform velocity of the lower layer. The distance along the survey that marks the transition from a curved to a linear time-distance profile is the *crossover distance*. In the time-distance plot, this intersection is indicated as the *crossover point* (Figure 4c). All first arrivals at geophones with distances greater than the crossover distance

have raypaths that travel from the surface along arcuate paths through the upper layer and intersect the lower, uniform velocity layer. The velocity contrast between the base of the upper layer and top of the lower layer causes the seismic rays to be refracted once again. Because no further refraction occurs within the lower, uniform-velocity layer, only seismic rays that are refracted along the transitional boundary (or reflected off the boundary) will return to the surface, whereas all rays that enter the lower layer will continue to greater depths and not return to the surface. Therefore, the first-arrival raypaths travel along the lower-layer interface, similar to a direct surface wave in a single uniform velocity layer. The rays then reach each successive geophone by reversing their initial arcuate path from depth back to the surface (Figure 4c). Because the raypaths of all first arrivals at distances greater than the crossover distance take the same amount of time to travel down to the lower-layer interface and back up to the surface (assuming a uniform thickness for this upper layer), the difference between arrival times at successive geophones is determined by the time required for the ray to travel the distance between geophones along the lower-layer boundary moving at the lower-layer velocity. This results in a linear time-distance profile at distances greater than the crossover distance (Figure 4c).

[19] The average velocity, V_{avg} , of the upper layer can be determined by taking the reciprocal of the slope of a line drawn in time-distance space from the origin through the crossover point (Figure 4c). Similarly, the velocity of the lower layer, V_m , can be determined by taking the reciprocal of the slope of the best fit linear trend to all first-arrival points beyond the crossover distance. The depth of the upper layer, h , can be determined by treating the data as a simple two-layer model with an upper-layer velocity of V_{avg} and a

lower-layer velocity of V_m , such that the depth is calculated as

$$h = \frac{t_o}{2} \left(\frac{V_m V_{avg}}{(V_m^2 - V_{avg}^2)^{1/2}} \right), \quad (1)$$

where t_o is the time intercept of the linear lower-layer trend in time-distance space (Figure 4c) [Sheriff and Geldart, 1982; Mussett and Khan, 2000]. If the upper-layer velocity increases linearly with depth, the velocity at any given depth can be calculated as

$$V(z) = V_o + az, \quad (2)$$

where $V(z)$ is velocity at depth z , V_o is the surface velocity, and a is the velocity gradient. If the surface velocity, V_o , and the velocity at the base of the upper layer, V_c , are known, then the velocity gradient, a , can be directly calculated as

$$a = \frac{(V_c - V_o)}{h}. \quad (3)$$

The time-distance profile for all points between the origin and the crossover point can be modeled as

$$t(x) = \frac{2}{a} \sinh^{-1} \left(\frac{ax}{2V_o} \right), \quad (4)$$

where $t(x)$ is the first-arrival time at geophone distance x [Sheriff and Geldart, 1982]. By substituting equation (3) into equation (4), we obtain

$$t(x) = \frac{2h}{(V_c - V_o)} \sinh^{-1} \left(\frac{x(V_c - V_o)}{2hV_o} \right), \quad (5)$$

which provides a predictive equation for determining the first-arrival time for distances less than the crossover point as a function of distance along the profile, the thickness of the upper layer, and the velocities at the surface and base of the upper layer. We can match the initial curved portions of time-distance profiles by implementing a parameter search for the values of V_o and V_c that yield the best fit to the measured data.

[20] Our model assumes a linear velocity gradient between the surface and the base of the upper layer. Although we do not argue that this assumption is strictly correct, Clarke and Burbank [2010] showed that our field data could be well-fit using polynomials with constant curvature, which implies a constant increase in velocity with depth [Sheriff and Geldart, 1982]. Although we suggest the assumption of a linear velocity gradient is reasonable for these study sites, we note that a similar approach could be applied with a nonlinear velocity gradient by changing the functional form of equation (2).

[21] The choice of the crossover point, however, strongly influences the depth and, therefore, the velocity gradient of the upper layer. The crossover point can be visually identified when large velocity differences exist between the base of the upper layer and the top of the lower layer (Figure 4c and Figure 5, profile iii). When velocity contrasts are small or if the upper layer grades to the velocity of the lower layer

(Figure 5, profiles i and ii), however, visually distinguishing the crossover point becomes more difficult. In order to remove any uncertainty associated with manually choosing the crossover point, we automated the model to determine the crossover point and velocity parameters that result in the best fit to the measured data. Through an iterative process, every first-arrival point along the survey is examined as a potential crossover point for which the model scrolls through all possible combinations of V_o and V_c (velocities at the surface and base of the upper layer, respectively) to find the best fit to the observed data. Modeled values of V_o range from 0.01 km/s to 7 km/s in intervals of 0.05 km/s, whereas values of V_c are examined at intervals of 0.1 km/s and are defined to always be greater than or equal to the surface velocity, V_o , and less than the lower layer velocity, V_m . V_m is determined from the linear fit to all measured points greater than the potential crossover point, or from the final three points in the profile when the potential crossover point exceeds the distance of the third-to-last point. The best model fit is determined by the combination of crossover point and velocity-structure that produces the lowest root-mean square error for the entire profile, calculated over both the curved and linear sections (Figure 5; see also auxiliary material).

[22] Our initial test of profile linearity limits implementation of the two-layer geometry in cases where the data are just as readily explained by a single, uniform-velocity layer, i.e., when a linear fit to the entire survey explains less than 95% of the variance. This strategy is intended to account for noise within both the natural system and our measurements. Even when the initial linearity criteria are not met, however, by assessing whether the best fit to the entire survey is found when the crossover point is set to the initial point along the time-distance profile (equivalent to setting the upper-layer depth to zero), the model is still capable of identifying a profile that is best characterized by a linear trend. Additionally, although none of our surveys displayed this behavior, by testing the scenario in which $V_o = V_c$, such that no velocity gradient exists within the upper-layer, the model is also capable of identifying a simple two-layer geometry in which a uniform low-velocity layer sits above a uniform higher-velocity layer.

[23] The best modeled fit to ~8% of the surveys predict unrealistically low initial velocities. In cases where the modeled initial velocity is less than that of a sound wave through air (0.33 km/s), we filter the data in order to eliminate these unrealistic velocities. Because we can envision no reasonable geologic scenario to produce such low velocities, we assume they result from non-geological sources, such as premature triggering of the timer or geophone malfunction. In such cases, we remove the first point in the time distance profile and treat the second point as the new initial point. This procedure is equivalent to removing a thin upper layer from the seismic profile and allows analysis of the remaining profile. The surveys are then remodeled based on the new shortened survey profile. Because we are concerned here with the characteristics of bedrock, removal of a thin anomalous upper layer allows for a more robust assessment of actual bedrock velocities.

[24] Modeled error for each profile was calculated as the summed residuals between modeled and observed first-arrival times divided by the total survey time. Average

Table 1. Field and Laboratory Seismic Survey Statistics and Average Modeled Velocity Data^a

Location	Number of Surveys	Average Survey Length (m)	Average Laboratory Velocity (km/s)	Average Upper-Layer Depth (m)	Average Upper-Layer Velocity Gradient (km/s/m)	Average Surface Velocity (km/s)	Average Velocity at Base of Upper Layer (km/s)	Average Lower Layer Velocity (km/s)	Percent Model Error ^b	Average Interlayer Velocity Offset (km/s)
<i>Fiordland</i>	67	38.3 ± 1.2	4.0 ± 0.2	-	-	-	-	-	-	-
Multilayer	45	39.2 ± 1.6	-	7.0 ± 0.5	0.21 ± 0.03	0.9 ± 0.1	2.1 ± 0.2	3.4 ± 0.2	2.2 ± 0.2	1.2 ± 0.2
Uniform single layer	22	36.5 ± 1.4	-	-	-	-	-	1.5 ± 0.2	4.8 ± 0.4	-
<i>Southern Alps</i>	42	32.4 ± 1.5	2.7 ± 0.3	-	-	-	-	-	-	-
Multilayer	11	35.5 ± 3.2	-	7.2 ± 1.1	0.18 ± 0.05	0.8 ± 0.1	1.9 ± 0.3	3.2 ± 0.4	1.8 ± 0.2	1.2 ± 0.3
Uniform single layer	31	31.3 ± 1.7	-	-	-	-	-	2.0 ± 0.2	3.6 ± 0.3	-

^aAll uncertainty is expressed as standard error.

^bPercentage of model error is calculated as the summed residuals between the modeled and observed first-arrival times divided by the total survey time.

modeled error for single- and multilayer profiles from both regions is <5% (Table 1), suggesting that our implemented subsurface model characterizes the measured seismic refraction surveys reasonably well (Figure 5 and auxiliary material). Based on the model results, we produce near-surface velocity profiles as a function of depth (equation (3)) for each seismic refraction survey (Figure 5).

3.2.1. Velocity Model Results

[25] Distributions of surveys characterized by multilayer versus single-layer profiles reveal stark contrasts between Fiordland and the Southern Alps (Figure 6). In Fiordland, 67% of the surveys are best characterized by a multilayer profile, whereas only 33% display linear time-distance trends, indicative of a single layer of uniform velocity, i.e., an upper-layer depth of 0 (Figure 6a). Conversely, in the Southern Alps, 74% of the seismic surveys are best modeled as a single, uniform-velocity layer, and only 26% display a multilayer profile (Figure 6b). This simple subdivision of the data suggests that bedrock in Fiordland is predominantly

characterized by depth-dependent profiles with significant velocity gradients within the upper layer, whereas bedrock in the Southern Alps appears to display more uniform characteristics with depth.

[26] Although Fiordland and the Southern Alps display striking contrasts in the prevalence of single- versus multilayer depth profiles, the distributions of the upper-layer characteristics for multilayer profiles are surprisingly similar, despite the different rock types. Both regions display similar upper-layer velocity-gradient distributions with mean velocity gradients of 0.21 ± 0.03 km/s/m for Fiordland and 0.18 ± 0.05 km/s/m for the Southern Alps (Figures 6a and 6b and Table 1). Likewise, the mean upper-layer depth in both regions is ~ 7 m (Figures 6c and 6d), with maximum depths reaching ~ 16 m in Fiordland and ~ 12 m in the Southern Alps. Although the percentage of multilayer profiles is considerably lower in the Southern Alps, no significant difference exists in the pattern of upper-layer

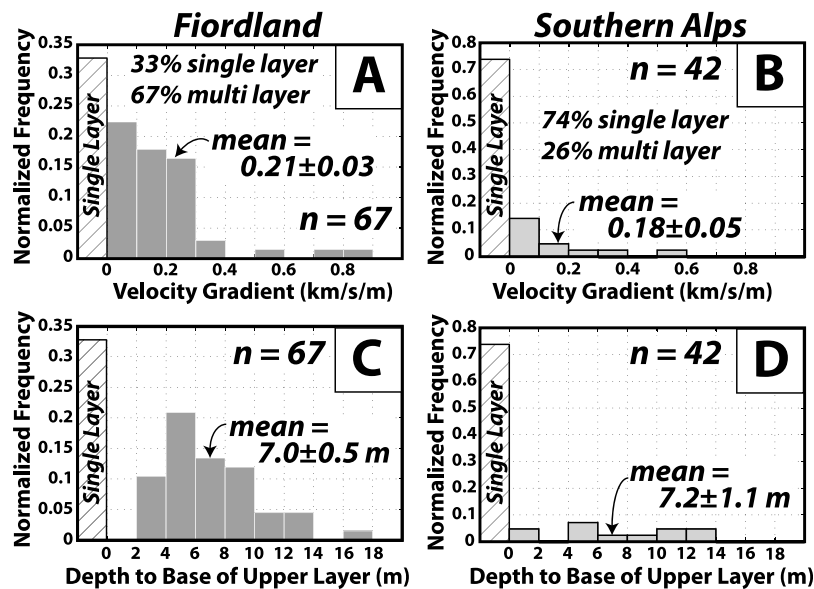


Figure 6. Model-determined upper-layer (a and b) velocity gradients and (c and d) depths. Results for surveys that are best modeled as single layers with uniform velocity (upper-layer depths and velocity gradients are both zero) are shown as striped bars, whereas distributions of surveys best characterized by the multilayer model are indicated by dark gray (Fiordland) or light gray (Southern Alps) bars. All means and standard errors are calculated for the multilayer models only. Note different frequency scales between Fiordland and Southern Alps plots.

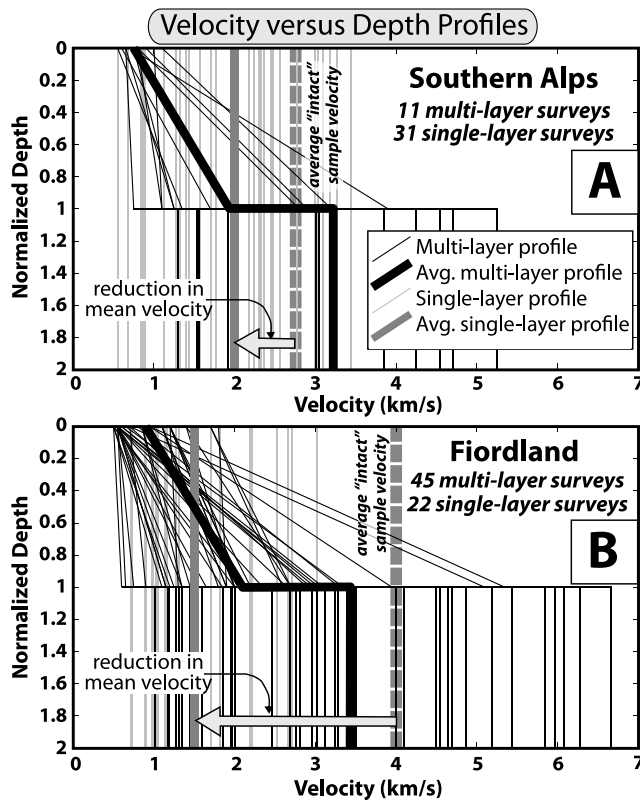


Figure 7. Normalized velocity versus depth profiles. Profile depths are normalized by the total thickness of the upper layer for (a) the Southern Alps and (b) Fiordland. Single-layer profiles produce a single vertical line (gray lines). Multilayer profiles show a linear velocity gradient from the surface to the base of the upper layer (normalized depth = 1), a discrete velocity offset along the transition between the two layers, and a uniform velocity within the lower layer (black lines). The average single-layer profile (thick gray line), the average multilayer profile (thick black line), and the average “intact” sample velocity from the laboratory measurements of hand samples (thick gray dashed line) are indicated for each region (uncertainty in the average velocity profile has been omitted for clarity but is shown in Table 1). Note the reduction (indicated by the open arrows) in average velocity for observed single-layer data versus average “intact” hand samples.

velocity gradient or depth distributions between the two regions. Similarly, no statistical differences exist in the velocity gradients or upper-layer depths between any of the individual rock types within either of the regions (see auxiliary material).

[27] Normalizing the depths of the velocity profiles by the depths to the base of the upper layer allows for direct comparisons of velocity profiles within either region and between the two regions (Figure 7). These normalized profiles allow us to examine the range of velocities within the upper and lower layers, as well as the magnitude of the velocity jump between layers. As expected, our results show wide variability in bedrock mechanical properties. Despite such variability, these large data sets allow us to identify both general trends within each region and contrasts between

them. To identify these regional trends, we determine the average normalized velocity profile and associated standard errors for both multilayer and single-layer profiles independently for each region (Figures 7a and 7b and Table 1).

[28] The average velocity of all single-layer profiles within the Southern Alps is 2.0 ± 0.2 km/s (Figure 7a). In Fiordland, despite the considerably faster ($\sim 50\%$) intact rock velocity, the average single-layer velocity is only 1.5 ± 0.2 km/s, $\sim 25\%$ slower than in the Southern Alps (Figure 7b). In both regions, profiles that are characterized by a single, uniform-velocity layer have maximum measured velocities less than ~ 3.5 km/s in the Southern Alps and ~ 3 km/s in Fiordland, whereas surveys with faster lower-layer velocities are consistently associated with multilayer profiles that show clear velocity gradients in the upper layer (Figure 7). The average multilayer profiles from both regions are remarkably similar (Figure 7 and Table 1): average upper-layer velocities in Fiordland and the Southern Alps grade from 0.9 ± 0.1 km/s and 0.8 ± 0.1 km/s at the surface to 2.1 ± 0.2 km/s and 1.9 ± 0.3 km/s at the base of the upper layer, respectively. The average lower-layer velocities show a similar equivalence of 3.4 ± 0.2 km/s in Fiordland and 3.2 ± 0.4 km/s in the Southern Alps. These average upper- and lower-layer velocities, in both regions, result in an average velocity offset at the interface between the upper and lower layer of 1.2 km/s (± 0.2 in Fiordland and ± 0.3 in the Southern Alps (Table 1)). Despite the similarity of the single- and multilayer velocity profiles in both ranges, the overwhelming dominance of single-layer profiles in the Southern Alps and multilayer profiles in Fiordland suggests stark contrasts in the average subsurface velocity structure between the two regions. Moreover, given the 1.5-fold difference in the mean intact bedrock velocities between these two regions (Figures 3 and 7 and Table 1), differences in subsurface characteristics must exist in order to produce the similar single- and multilayer average velocity profiles.

3.2.2. Causes of Subsurface Velocity Variation

[29] Our velocity model allows for inversion of seismic refraction surveys to quantify depth-dependent velocity variations within the subsurface of each survey site. Although the velocity profiles provide an integrated measure of subsurface properties, the particular causes of velocity variation are more difficult to isolate. Because all seismic surveys were conducted directly on bedrock surfaces with thin to absent soil cover, variations in seismic velocity are primarily interpreted to reveal changes in fracture density with depth. Yet, survey geometry, groundwater levels, soil cover, and seismic anisotropy due to foliation planes or preferential fracture orientations can also influence the measured seismic velocities. Additionally, differences in survey lengths may result in differences in the analyzed scale, depth, and resolution of seismic profiles, which may bias comparisons of individual or normalized surveys. Although the influence of these factors on our data could not be quantitatively constrained, we tried to minimize their influence through strategic field site selection and are able to qualitatively rule out many of these influences based on post-processing assessment of the data.

[30] Seismic velocity through a rock mass is greatly reduced by bedrock fractures [Sjogren *et al.*, 1979; Hudson, 1980; El-Naqa, 1996; Boadu, 1997; Kahraman, 2001; Leucci and De Giorgi, 2006; Fratta and Santamarina, 2002;

Cha et al., 2009]. Because the p-wave velocity gives an integrated measure of all material within the rock mass, however, material that fills fracture spaces will affect the velocity magnitude [*Fratta and Santamarina*, 2002; *Jaeger et al.*, 2007; *Cha et al.*, 2009]. Therefore, fractures that are filled with water will yield faster rock mass velocities than when filled with air. The effect of a subsurface groundwater level in uniformly fractured bedrock would be two linear and intersecting trends in time-distance space, with the first steep trend (slow velocity) correlating to bedrock with air-filled fractures from the surface down to the top of the groundwater level and a second, shallower trend (faster velocity) corresponding to regions below the water table (as in a simple, two-layer seismic refraction problem from any introductory geophysics text [see, e.g., *Mussett and Khan*, 2000, p. 69]). Thick ($\geq 1\text{--}5$ m), low-velocity soil cover above high-velocity bedrock surfaces would produce a similar pattern in time-distance space with a distinct break in slope between two linear sections. Yet, none of our surveys from either region display this characteristic pattern (Figure 7). Instead, these data suggest that thick, low-velocity cover and groundwater levels have a minimal influence on our survey profiles.

[31] Combinations of varying cover, water levels, and/or variations in fracture space with depth or along the profile, however, may result in far more complicated time-distance profiles, in which it would be difficult to distinguish the influence of bedrock fracturing from these alternative factors without more sophisticated subsurface seismic and hydrological models, or direct observation from drill cores. We tried to minimize these influences by collecting all surveys as directly as possible on bedrock outcrops with minimal cover and on clear days, when groundwater levels would be absent or at their lowest levels. Nonetheless, some surveys were collected the day after storms, and minimal surface cover could not be avoided at all locations.

[32] Seismic anisotropy due to preferential orientation of crystalline properties, e.g., mineral grains and foliation planes, or aligned fracture sets can have a strong influence on the magnitude of p-wave velocities [*Sjogren et al.*, 1979; *Hudson*, 1981; *Brocher and Christensen*, 1990; *Pyrak-Nolte et al.*, 1990b; *Schoenberg and Sayers*, 1995; *Vilhelm et al.*, 2010]. Because large-scale stress fields predominantly control the orientation of foliation, we expect anisotropic orientations to remain roughly uniform (both laterally and with depth) over the meter scales of our seismic surveys. Therefore, the overall magnitude of the p-wave velocity would be affected uniformly, and depth-dependent variations in p-wave velocity and profile curvature would still need to be attributed to another source, such as an increase in the density of fractures, rather than to changes in the orientation of fractures or foliation. If, on the other hand, the anisotropic orientation varies along the length or depth of the survey, then we would expect variations in p-wave velocity along the profile.

[33] In an attempt to minimize uncertainty due to seismic anisotropy, we chose survey sites where foliation (when present) was visible, and conducted surveys along linear paths that maintained near-perpendicular orientations to foliation and fracture planes along the full survey length. Additionally, lab samples were cut and measured perpendicular to foliation (when present) to allow for direct

comparison between laboratory measurements and their associated field sites. The effect of changes in seismic anisotropy should be most prevalent in the weak, highly foliated bedrock of the Southern Alps, rather than in Fiordland, which comprises more isotropic igneous and orthogneissic bedrock [*Mason*, 1962; *Bradshaw*, 1990; *Okaya et al.*, 1995; *Eberhart-Phillips and Reyners*, 2001; *Stern et al.*, 2001]. Yet, the Southern Alps surveys are overwhelmingly dominated by near linear profiles, which preclude subsurface changes in velocity due to changes in anisotropic orientation. If the few Southern Alps profiles with significant curvature are due to foliation-induced changes in anisotropy, as opposed to gradients in fracture density, this condition would only strengthen our assertion that, in the Southern Alps, subsurface fracture characteristics are predominantly uniform with depth. Conversely, in Fiordland, the gneissic and granitic rock is expected to be more seismically isotropic (especially over the meter-scales examined here) and produce fast, uniform-velocity profiles in the absence of fracturing or weathering gradients; yet, this region is dominated by multilayer profiles with strong velocity gradients within the upper layer. Given that the predominant patterns of subsurface velocity in both Fiordland and the Southern Alps run counter to predictions for the influence of changes in anisotropic orientation, these data suggest that changes in anisotropy have a minimal influence on our seismic profiles and that changes in velocity magnitude are more likely to have arisen from variations in the density of bedrock fractures.

[34] Uncertainties and inter-survey variability associated with survey geometry and the inherently noisy field environment may also influence seismic-velocity inversion from field data. Surface undulations and/or minor errors in geophone spacing that change the survey geometry relative to the model configuration, as well as thin surface cover that influences near-surface velocity and geophone contact with bedrock, may have a localized influence on individual geophone readings. In addition to filtering unrealistically low initial velocities (<0.33 km/s), use of best fit regressions to entire curved or linear sections of a profile, as opposed to calculating the instantaneous velocity based on the slope between two consecutive points, helps smooth and minimize the influence of noise or individual geophone anomalies and focuses velocity assessment on trends defined over longer survey reaches. Additionally, the length of a seismic survey dictates the scale of integrated measurement and the potential depth of analysis. Because all surveys used a similar number of evenly spaced geophones, the survey length also controls geophone spacing and thus the analysis resolution. Therefore, long surveys analyze larger scales and greater depths, but sacrifice resolution, whereas short surveys provide higher resolution of the very shallow subsurface, but limit the depth and scale of analysis. Although the influence of survey scale can be important, post-processing analysis suggests that scaling issues have a minimal influence on our data set (see auxiliary material).

[35] Based on the location of the survey sites directly on bedrock surfaces and on the post-processing assessment of the velocity profiles, we suggest that thick soil cover, groundwater levels, variations in seismic anisotropy, and uncertainty associated with survey geometry have minimal affects on the modeled velocity profiles. We, therefore,

assume that the observed depth-dependent velocity variations within these profiles are primarily due to variations in bedrock fracture density within the shallow subsurface.

3.2.3. Velocity Reductions Due to Bedrock Fractures

[36] All velocity profiles are assumed to represent the integration of intact bedrock velocity and velocity reductions by bedrock fractures [Hudson, 1981; Berryman, 2007; Jaeger et al., 2007; Cha et al., 2009]. Consequently, we assess fracture-induced velocity reductions by calculating the difference between the intact-bedrock velocities and the model-derived velocity profiles. The magnitude of the velocity reduction, at any given depth, is dependent on the density of bedrock fractures, such that large reductions correspond to higher fracture densities, and vice versa [Sjogren et al., 1979; Hudson, 1980, 1981; El-Naqa, 1996; Boadu, 1997; Kahraman, 2001; Fratta and Santamarina, 2002; Leucci and De Giorgi, 2006; Cha et al., 2009]. Average velocity reductions were calculated from the average single- and multilayer velocity profiles relative to the average intact bedrock velocity for both regions (Figure 7 and Table 1). In Fiordland, the average single-layer velocity is reduced by >2.6 km/s relative to the average intact velocity of ~ 4 km/s (Figure 7b). The average multilayer profile in Fiordland is reduced by a modest ~ 0.6 km/s within the lower layer, but displays considerably larger reductions in the upper layer ranging from ~ 3 km/s at the surface to ~ 2 km/s at its base. Conversely, in the Southern Alps, the average single-layer profile is only reduced by ~ 0.7 km/s (Figure 7a). The average multilayer profile is reduced by ~ 2 km/s at the surface and ~ 0.7 km/s at the base of the upper layer. Notably, the velocity of the average lower layer in the Southern Alps is ~ 0.5 km/s greater than the average intact velocity (Figure 7b and Table 1). Therefore, the 26% of Southern Alps surveys characterized by multilayer profiles appear to have lower-layer velocities that, on average, are faster than the average intact velocity measured in hand samples.

[37] Because the intact velocity at each field site is assumed to be invariant with depth, the modeled velocity gradients are interpreted to result from gradients in bedrock-fracture densities, whereas the distinct jump in velocity at the interface between the modeled layers identifies a sharp drop in the density of bedrock fractures between the base of the upper layer and the top of the lower layer. The uniform velocity in the lower layer is attributed to either unfractured homogeneous bedrock or to uniformly fractured rock. Based on these interpretations, we argue that our seismic data provide a quantitative metric to assess the relative density and depth of bedrock fractures, which in turn, may directly relate to hillslope-scale rock mass strength and bedrock erodibility [Deere, 1964; Sjogren et al., 1979; Selby, 1980, 1992; Hack, 2000].

3.3. Quantifying Bedrock-Fracture Density

[38] Reductions in the seismic velocity of fractured versus intact bedrock can be used to quantify fracture characteristics through use of *effective-medium models* [Sjogren et al., 1979; Hudson, 1980, 1981; Schoenberg and Sayers, 1995; Jaeger et al., 2007]. Effective-medium theory considers the rock mass as a continuum in which velocity reductions result from a holistic reduction in the effective-elastic moduli over the entire length-scale of the velocity mea-

surement. Effective-medium models utilize seismic-wavelengths that are much longer than the length-scale typified by individual fractures or inter-fracture spacing and, therefore, provide a frequency-independent, integrated measure of both the intact and fractured portions of the rock mass [Hudson, 1980, 1981; White, 1983; Schoenberg and Sayers, 1995; Cha et al., 2009; Zhang et al., 2009].

[39] We develop a simplified, effective-medium model in which we assume that seismic waves propagate normal to fracture planes and that the seismic-wavelength is much longer than the length-scale and spacing of bedrock fractures. The model calculates the volumetric fracture density, i.e., the volume of fracture space within the rock mass, required to reduce the intact bedrock velocity such that it equals the velocity measured through the entire rock mass.

[40] The assumption of seismic wavelengths that are much longer than the scale and spacing of fractures is appropriate for the field-based surveys presented here, in which the seismic source (a sledgehammer striking a steel plate) produces propagating waves with common wavelengths ranging between ~ 3 and ~ 12 m (corresponding to frequencies of ~ 500 – 2000 Hz for velocities of up to ~ 6 km/s) [Keiswetter and Steeples, 1995; Mussett and Khan, 2000; Vilhelm et al., 2010]. The assumption of wave propagation normal to fracture planes, however, is not strictly true in most field settings [Schoenberg and Sayers, 1995; Cosgrove, 1998; Liu et al., 2000]. Based on our simple field-survey geometry, this assumption would require vertical fracture planes striking orthogonally to the survey direction [Hudson, 1980, 1981; Hack, 2000; Fratta and Santamarina, 2002; Cha et al., 2009]. Fracture orientations aligned obliquely to the survey direction would influence the rock mass velocity and the model-derived volumetric fracture density. Aligned fracture sets produce seismic anisotropy, with the fastest direction parallel to fracture orientation (where the wave travels through intact rock parallel to the fracture planes) and the slowest direction perpendicular to fracture planes [Pyrak-Nolte et al., 1990b; Schoenberg and Sayers, 1995]. Seismic velocities increase nonlinearly as the angle between the fracture plane and the propagation direction approaches parallel alignment [Pyrak-Nolte et al., 1990b]. Therefore, because the model assumes wave-propagation normal to fracture planes, surveys conducted obliquely to the fracture orientation would yield faster rock mass velocities than expected and would give the appearance of lower volumetric fracture densities. Conversely, reductions in velocities and the effective-elastic moduli of the rock mass can occur that are not directly caused or accompanied by increases in fracture volume. Fractures formed under shear strain (as opposed to opening-mode fractures) can reduce the strength and elasticity of the rock mass without producing significant increases in fracture space. Additionally, intersecting fractures that completely detach rock fragments can significantly reduce the elastic moduli and velocity of the rock mass without producing a proportional increase in fracture space [Schoenberg and Sayers, 1995; Cosgrove, 1998; Liu et al., 2000]. Although these factors may not significantly or proportionally increase the amount of fracture space within the rock mass, based on our simple model assumptions, the consequent reductions in the effective-elastic moduli and rock mass velocity would still result in an apparent increase in the model-determined volumetric fracture density.

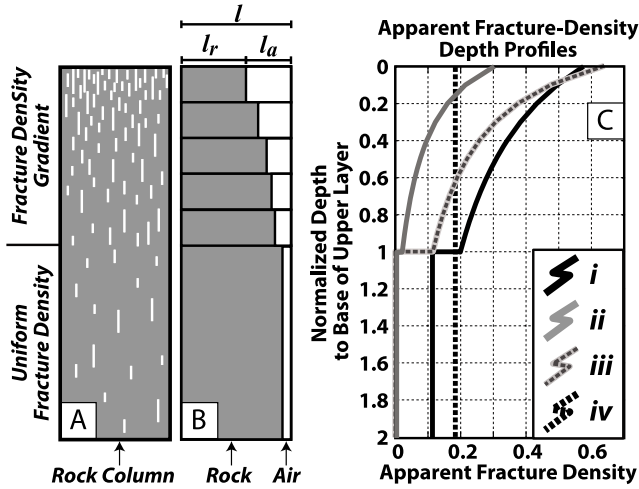


Figure 8. Schematic illustration of the apparent fracture-density model. Starting with (a) a fractured column of rock, the model considers (b) the unit volume of rock and the unit volume of air-filled fracture space that would be required in order to reduce the intact rock velocity to be equivalent to the measured field-velocity at any given depth. (c) Examples of normalized apparent fracture-density depth profiles for the four surveys of Figure 5.

[41] When the orientation and character of bedrock fractures can be well constrained, e.g., by detailed field observations of exposed bedrock or by borehole measurements, effective-medium models can be adjusted to account for complex fracture orientations, multiple fracture sets, or alternative influences on the effective elastic moduli [Schoenberg and Sayers, 1995; Liu *et al.*, 2000; Zhang *et al.*, 2009]. When fracture characteristics and orientations are not well constrained, however, application of our simple effective-medium model will underestimate the volumetric fracture density for surveys conducted oblique to fracture orientations and overestimate the volumetric fracture density if the rock mass is highly influenced by very thin or intersecting fractures that reduce the effective-elastic moduli without a proportional increase in fracture volume.

[42] Although we attempted to measure surveys perpendicular to foliation and fracture orientations, detailed surface and subsurface constraints on fracture orientation and the potential influence of multiple fracture-sets remain unknown. We suggest that our data primarily represent seismic measurements taken near-perpendicular to fracture planes, but we caution that uncertainty in our data could lead to either over- or under-estimates of the true volumetric fracture density. Therefore, in the context of these uncertainties, we consider the application of our simple effective-medium model as providing a quantitative measure of the *apparent volumetric fracture density*.

3.3.1. Apparent Volumetric Fracture-Density Model

[43] In order to quantify the apparent volumetric fracture density with depth (hereafter referred to simply as the apparent fracture density), we use the model-derived subsurface velocity profiles (Figure 7) and the laboratory measurements of intact p-wave velocities for each survey site (Figure 3). Assuming that the estimated intact velocity is

equivalent to the velocity in unfractured rock, the model determines the volumetric fracture density with depth required to produce the subsurface velocity profiles. In general, subsurface p-wave velocities are slower than the measured velocities of intact rock (Figures 3 and 7). In 20% of the surveys, however, the lower-layer velocity, V_m , is greater than the velocity of the associated hand sample. This contrast is not surprising given that the surface material from which hand samples were collected is more exposed to weathering processes or may contain more micro-fractures, either from natural causes or due to fracturing during collection. Additionally, surface bedrock characteristics might actually vary from that of the bedrock found several meters deeper. In the cases where V_m is greater than the laboratory velocity measurement, we define V_m as the best estimate of intact rock velocity. Because both the lower-layer velocity and the intact hand-sample velocity measurements can be influenced by weathering, micro-fractures, or other localized discontinuities that cannot be completely assessed, we consider our estimates of intact rock velocity from either hand samples or V_m to be minimum estimates.

[44] We analyze each survey as a characteristic rock column with a fracture pattern that produces the measured velocity profile (Figure 8a). Instead of treating this column as rock with distributed fractures that increase in density toward the surface, we consider separately the amount of rock space versus the amount of fracture space for any given horizontal slice through the column (Figure 8b). The p-wave velocity through this column cross-section is equal to the horizontal unit length, l , of the column divided by the time it takes the p-wave to travel through it [Hudson, 1980, 1981; Schoenberg and Sayers, 1995; Cha *et al.*, 2009]. Therefore, the velocity, V , through a horizontal slice at a given depth can be calculated as

$$V = \frac{(l_r + l_f)}{(t_r + t_f)}, \quad (6)$$

where l_r and l_f are the associated lengths of rock and fracture space, respectively, that sum to the total cross-sectional length l . Similarly, t_r and t_f are the times required for the p-wave to travel through the respective mediums. The time, t_i , spent in either medium (where the subscripted i can be replaced with either r or f) can be expressed as

$$t_i = \frac{P_i l}{V_i}, \quad (7)$$

where P_i is the fraction of the unit length, l , composed of either rock or fracture space and V_i is the p-wave velocity through that medium. Substitution of equation (7) into equation (6) yields

$$V = \frac{(P_r l + P_f l)}{\left(\frac{P_r l}{V_r} + \frac{P_f l}{V_f}\right)}. \quad (8)$$

By substituting $P_r = 1 - P_f$ into equation (8), the velocity at a given depth in the rock column can be determined by

$$V = \frac{V_r V_f}{(V_f - V_f P_f + V_r P_f)}. \quad (9)$$

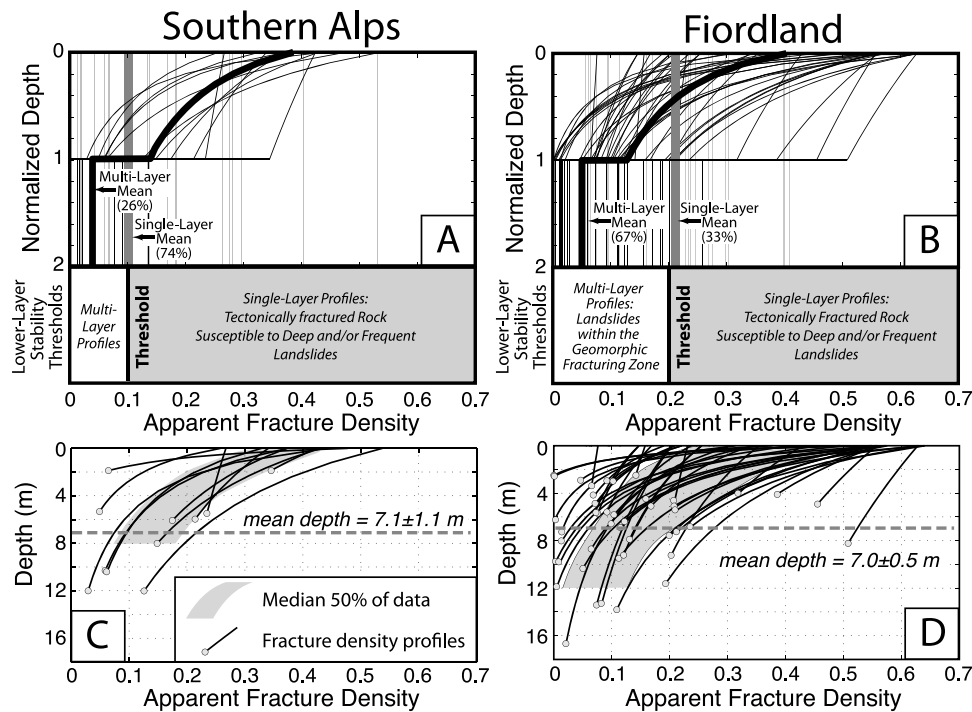


Figure 9. Apparent fracture density versus depth profiles. Depth-normalized apparent fracture-density profiles for (a) the Southern Alps and (b) Fiordland. Multilayer profiles are indicated as black lines, with the average multilayer profile displayed as the thickest black line. Single-layer profiles are displayed as gray vertical lines with the average single-layer profile identified by the thickest gray line. Uncertainty in the average apparent fracture-density profiles has been omitted for clarity but is displayed in Table 2. Note that all multilayer profiles contain an offset in apparent fracture density at the base of the upper layer. The lower panels in Figures 9a and 9b illustrate the fracture-density stability thresholds of $\sim 10\%$ in the Southern Alps and $\sim 20\%$ in Fiordland. These thresholds differentiate between highly fractured, unstable bedrock prone to deep and/or frequent landslides, which leave behind uniform single-layer profiles, and less fractured, more stable rock, in which geomorphic fractures develop over time and landslides typically occur at depths within this geomorphically fractured zone. (c and d) Apparent fracture density as a function of the true modeled depth for the upper layer of each multilayer profile.

We rearrange equation (9) to solve for the fraction of the unit length occupied by fracture space, such that

$$P_f = \frac{V_f}{(V_r - V_f)} \left(\frac{V_r}{V} - 1 \right). \quad (10)$$

Therefore, based on the subsurface velocity through the rock mass (V), the intact rock velocity (V_r), and the estimated velocity of the fracture-filling material (V_f), we can determine the relative fractions of rock (P_r) and fracture space (P_f) at any given depth through the rock column (Figure 8c). In three-dimensional space, P_r and P_f represent the volumetric density of rock and fracture space, respectively, as a fraction of the unit rock mass volume at a given depth.

[45] For all of our surveys, we assume that the fracture space is entirely air filled, with a velocity of 0.33 km/s. Although our assumption of air-filled fracture space may be reasonable for these profiles, the model could easily be modified to incorporate the influence of groundwater or other fracture-filling material over varying depths.

3.3.2. Apparent Volumetric Fracture-Density Results

[46] Our model results suggest that linear velocity gradients in the shallow subsurface are caused by nonlinear

declines in apparent fracture density with depth (Figures 8c and 9). This relation arises from the proportionality between the apparent fracture density, P_f , and the reciprocal of the velocity through the rock mass at a given depth, $1/V$, (equation (10)). Thus, the magnitude of the linear velocity gradient is controlled by the degree of nonlinearity in the fracture-density depth profile. We use depth-normalized profiles of apparent fracture density to compare the wide range of survey results (Figures 9a and 9b) such that normalized depths between 0 and 1 are related to the modeled upper layer, whereas normalized depths >1 correspond to the lower model layer. For linear time-distance profiles with no upper layer, the normalized apparent fracture-density profile is uniform with depth and is simply the fracture density calculated using the measured field velocity and the estimated intact rock velocity (equation (10)).

[47] In order to summarize the wide range of apparent fracture-density profiles and identify general trends, we calculate the average apparent fracture-density profile and standard errors for both multilayer and single-layer profiles for Fiordland and the Southern Alps (Figure 9 and Table 2). These profiles identify some stark contrasts between the two regions, as well as some similarities that are surprising,

Table 2. Average Apparent Fracture Density Data^a

Location	Number of Surveys	Average Apparent Fracture Density at Surface	Average Apparent Fracture Density at Base of Upper Layer	Average Lower Layer Apparent Fracture Density	Average Interlayer Apparent Fracture-Density Offset (Percent Change Between Layers)
<i>Fiordland</i>					
Multilayer	45	0.40 ± 0.03	0.13 ± 0.02	0.05 ± 0.01	0.07 ± 0.01 (60%)
Uniform single layer	22	-	-	0.21 ± 0.03	-
<i>Southern Alps</i>					
Multilayer	11	0.39 ± 0.03	0.14 ± 0.03	0.04 ± 0.01	0.10 ± 0.03 (70%)
Uniform single layer	31	-	-	0.1 ± 0.03	-

^aAll uncertainty is expressed as standard error.

given the major differences in underlying rock types. In the Southern Alps, the average single-layer profile, derived from 74% of the surveys, has a uniform apparent fracture density of 0.1 ± 0.03 (Figure 9a and Table 2). This apparent density indicates that, on average, ~10% of the total volume within these single-layer profiles is occupied by fracture space and that this apparent fracture density remains uniform to depths beyond the resolution of the seismic surveys. In Fiordland, the average single-layer apparent fracture density, derived from 33% of the total regional profiles, is 0.21 ± 0.03 (Figure 9b): twofold greater than in the Southern Alps. The average multilayer profiles from both regions have remarkably similar apparent fracture densities (Figures 9a and 9b and Table 2). For multilayer profiles in Fiordland and the Southern Alps, fractures, on average, appear to account for $40 \pm 3\%$ and $39 \pm 3\%$ of the volume at the surface, respectively. Apparent fracture densities decrease non-linearly with depth from the surface to the base of the upper layer where fractures appear to account for $13 \pm 2\%$ of the total volume in Fiordland and $14 \pm 3\%$ in the Southern Alps. Apparent fracture densities within the average lower layer occupy only $5 \pm 1\%$ of the volume in Fiordland and $4 \pm 1\%$ in the Southern Alps. These calculations reveal abrupt and significant decreases in the average, apparent fracture density across the upper-to-lower layer boundary of ~60% and ~70%, respectively.

[48] Although the fracture profiles are widely variable, examination of apparent fracture density as a function of true modeled depth for the upper-layer of all multilayer profiles (Figures 9c and 9d) reveals similar fracture patterns with gradients that extend to average depths of ~7 m in both regions (Table 2). Overall, these results show that uniformly fractured single-layer profiles in Fiordland contain apparent fracture densities that, on average, are twofold greater than in the Southern Alps. Conversely, despite the different rock types, multilayer profiles from both regions display nearly identical apparent fracture-density profiles.

[49] Whereas our methodology is straightforward, the results should be viewed in the context of several uncertainties and caveats. In comparison to our simplified model assumptions, the complexity of actual survey sites may result in unconstrained errors in calculated fracture densities, particularly in the very near surface. We note that actual volumetric fracture densities (or porosity) in excess of 50% are probably unrealistic except for in the most porous pumice or uncompacted muds. Therefore, we infer that survey profiles with apparent fracture densities at the surface

greater than ~50% are most likely influenced by soil, regolith, or other sedimentary cover with low seismic velocities that cause our calculated apparent fracture densities to be anomalously high (Figure 9). Because bedrock cropped out along every survey site and in most cases geophones were placed directly in contact with bedrock, the influence of low-velocity surface cover is believed to be contained within the upper few meters and localized to lateral extents spanning only a few geophones (2–10 m). Therefore, velocity profiles and apparent fracture densities from depths below this surface cover still yield robust results. Although extreme, near-surface apparent fracture densities (>50%) should be viewed with skepticism, the influence of low-velocity surface material appears limited to the topmost 1–2 m (Figure 9) and only influences a small fraction of our field surveys.

[50] Our method provides a simple means of using velocity profiles to quantify depth-dependent, apparent volumetric fracture densities within the shallow subsurface. The method does not, however, allow for independent determination of fracture orientation, spacing, or other characteristics, e.g., lengths, widths, or roughness. Additionally, the model does not distinguish between a small number of large/wide fractures or a large number of small fractures, even though such differences may influence hillslope strength and stability. Alternative field-based techniques to assess subsurface characteristics based on s-wave splitting, displacement-discontinuity models, or 3-D survey methods are capable of producing higher resolution subsurface data and extracting information on individual fracture characteristics [Pyrak-Nolte et al., 1990a, 1990b; Crampin and Lovell, 1991; Boadu and Long, 1996; Heincke et al., 2006; Berryman, 2007; Bansal and Sen, 2008; Renalier et al., 2010]. These alternative methods, however, require significantly more elaborate and time-consuming field campaigns with far more cumbersome survey equipment, as well as more complex modeling, inversion, and interpretation techniques. Such elaborate campaigns generally limit their application to a single, easily accessible field site. The major benefit of our approach is the simplicity of conducting the field surveys, with a portable seismograph and sledgehammer source, and the ease of applying our inversion models to quantify depth-dependent patterns of p-wave velocities and apparent volumetric fracture densities within the shallow subsurface. Our proposed technique allows for numerous surveys to be conducted efficiently (both temporally and financially), even in remote and/or rugged terrain, and it provides a means by which to

quantitatively assess hillslope-scale bedrock mechanical properties and patterns of subsurface fracturing.

4. Discussion

[51] By probing the shallow subsurface with short seismic arrays, we have attempted to derive new quantitative data on the seismic velocity structure and related fracture patterns within the upper few meters of bedrock. As with most field-based assessments of bedrock characteristics, our data show wide variability in rock mass properties, which further highlights the necessity of analyzing large data sets in order to accurately differentiate regional trends. Overall, our results from more than 100 surveys show that bedrock in both Fiordland and the Southern Alps of New Zealand is characterized either by pervasive, uniform fracturing over the full depth of the profile or by severe, differential fracturing within a near-surface rock mantle that directly overlies uniformly, but considerably less fractured bedrock at depth (Figures 7 and 9). In the Southern Alps, bedrock is overwhelmingly characterized by uniform and pervasive fracturing, with three-quarters of the surveys being best modeled as uniform, single-layer profiles, whereas only one-quarter of the surveys are best modeled as multilayer profiles with an upper, more densely, but differentially fractured layer. Conversely, in Fiordland, two-thirds of the surveys display an upper, differentially fractured layer that overlies a uniformly fractured layer at depth, whereas only one-third of the Fiordland surveys display uniform fracture patterns over the full depth of the profile (Figures 6, 7, and 9). When the two ranges are compared, their contrasting proportions of single- versus multilayer fracture styles suggest striking differences in subsurface characteristics.

[52] Based on the bimodal patterns of bedrock fracturing within both regions, we propose two independent fracturing mechanisms to produce the observed subsurface profiles: (1) tectonic fracturing and (2) geomorphic fracturing. Bedrock from both the full, single-layer profiles and from the lower layer of the multilayer profiles appears uniformly fractured to depths greater than the resolution of these short seismic surveys. We suggest that this uniform pattern of bedrock fracturing is most readily attributed to tectonic processes. As tectonic forces fold and bend rocks, bedrock fractures form in order to accommodate the imposed strain [Molnar *et al.*, 2007]. Tectonic fracturing can result in spatially extensive, pervasive fracturing to great depths and would be expected to produce a subsurface profile with relatively uniform velocity and fracture density. Conversely, in the differentially fractured upper layers of the multilayer profiles, bedrock fractures are most abundant at the surface and decrease with depth (Figure 9). Although we expect a modest reduction in fracture volume with depth due to increased lithostatic pressure, the thin (<15 m) lithostatic loads observed here would be insufficient to cause the significant decreases in fracture space required to produce either the strong velocity gradients within the upper layer or the sharp velocity contrasts observed at the boundary between the upper and lower layers [Miller and Dunne, 1996; Hoek and Bray, 1997; Jaeger *et al.*, 2007]. Additionally, we would expect increases in lithostatic pressure to have a similar influence on all profiles, yet our single-layer profiles show no evidence of pressure-induced increases in

velocity or reductions in apparent fracture density. We, therefore, suggest that geomorphic processes focused within the near surface produce the depth-dependent fracture gradients (Figures 9c and 9d). Fracturing driven by thermal, chemical, or biotic processes would be expected to propagate from the surface down to shallow depths [Walder and Hallet, 1985; Anderson, 1998; Hales and Roering, 2005, 2007, 2009; Anderson *et al.*, 2007; Gabet and Mudd, 2010]. Additionally, internal stresses produced by topographic relief or surface curvature may further drive fracturing within the shallow subsurface [Augustinus, 1992b, 1995; Miller and Dunne, 1996; Martel, 2006]. This surface-down geomorphic-fracturing would be expected to produce a subsurface profile with an exponentially decreasing fracture density caused by the attenuation of surface-process efficiency with depth. Consequently, we propose that the velocity and apparent fracture-density depth profiles presented here reveal signatures of both geomorphic and tectonic fracturing processes (Figures 7 and 9).

[53] Within the multilayer profiles, the interface between the upper and lower layers can be interpreted as a boundary between these two process domains. The depth of this boundary, delineated by the depth to the offset in both the velocity and apparent fracture-density profiles, identifies both a strong contrast in mechanical properties and a possible limit to the extent of near-surface geomorphic fracturing. This depth, however, most likely represents a dynamic balance between the rate of surface-down fracture propagation, which increases the interface depth, and the rate of erosion, which reduces the boundary depth. Therefore, the formation and preservation of depth-dependent fracture gradients will differ from site to site depending on the rates of geomorphic fracturing and the removal of upper parts of the profile by erosion (Figure 10).

[54] Strong correlations have been shown between seismic-wave velocities, the density of bedrock fractures, and semi-quantitative engineering classifications of rock mass strength [Sjogren *et al.*, 1979; El-Naqa, 1996; Budetta *et al.*, 2001; Kahraman, 2001; Leucci and De Giorgi, 2006; Cha *et al.*, 2009]. Such correlations are not surprising given that both seismic velocity and rock mass strength classifications take into account the competency of intact bedrock and the density and characteristics of bedrock fractures. Although we do not know the precise functional relationship between rock mass strength and fracture density, for any given intact rock, increased fracture densities are expected to cause a concurrent decrease in the rock mass strength as a whole [Selby, 1980, 1992; Moon and Selby, 1983; Bieniawski, 1989; Schmidt and Montgomery, 1995; Hoek and Brown, 1997; Jaeger *et al.*, 2007]. Therefore, to the extent that fracture density modulates rock mass strength at hillslope scales, the apparent fracture-density depth profiles can be considered in the context of rock mass strength.

[55] The intrusive igneous and high-grade metamorphic rocks in Fiordland [Bradshaw, 1990] are presumed to be intrinsically stronger than the low-grade schists and greywacke/argillite of the Southern Alps [Augustinus, 1992a], and they clearly display faster intact seismic velocities (Figures 3a and 3b). Typical compression strengths for granites range between ~100–200 + MPa, whereas schists can have compression strengths upwards of ~100 MPa, but more typically reveal strengths <50 MPa [Rahn, 1996; Hoek

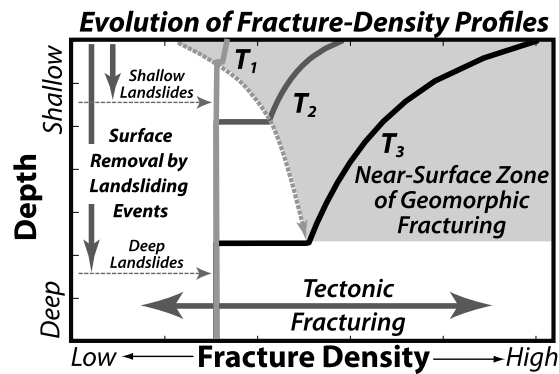


Figure 10. Evolution of fracture-density depth profiles. Although tectonic fracturing modulates fracture densities at depth, bedrock fracturing within the shallow subsurface is dependent on the efficiency of geomorphic fracturing processes, the duration of these processes, and the rate and style of surface erosion. Slow erosion rates or long intervals between landslides allow deeper geomorphic fracture profiles to develop (T_1 , T_2 , and T_3 represent profiles of increasing age), whereas rapid erosion rates remove surface material before geomorphic fractures can develop. Similarly, shallow landslides may only remove a small portion of the geomorphically fractured material, while large, deep landslides may penetrate to depths far beyond the extent of geomorphic fractures.

and Bray, 1997; Jaeger *et al.*, 2007]. Yet, despite their contrasting rock types and order-of-magnitude differences in rock uplift rates, both Fiordland and the Southern Alps reveal similar modal hillslope angles of $\sim 32^\circ$ [Clarke and Burbank, 2010]. Such similarity implies that both regions are characterized by threshold slopes with equivalent hillslope-scale rock mass strength. Our seismic analyses now suggest how this equivalence may be achieved. First, single-layer profiles in Fiordland have average apparent fracture densities that are twofold greater than those of the Southern Alps (Figure 9 and Table 2). Second, and perhaps of more significance to surface slopes, is the difference in the predominant surface characteristics of both regions. In the Southern Alps, three-quarters of the profiles display apparent fracture densities at the surface that on average account for $\sim 10\%$ of the total volume. In contrast, in Fiordland, two-thirds of the profiles reveal average apparent fracture densities at the surface of $\sim 40\%$: fourfold greater than in the Southern Alps. Our results, therefore, suggest that higher fracture densities within the intrinsically stronger Fiordland rocks yield equivalent rock mass strengths to those of the less densely fractured, but intrinsically weaker Southern Alps rocks. This result supports the contention that the primary factor governing threshold slope angles is the mechanical strength of the landscape surface [Clarke and Burbank, 2010]. Our data also support the interpretation of threshold angles of stability as representing a balance between intact rock strength and the reduction of that strength due to the density of surface fracturing [Selby, 1992; Schmidt and Montgomery, 1995; Clarke and Burbank, 2010]. We argue that the same principles should apply throughout the rock column, such that the rock mass

strength at any given depth is dependent on the intact rock strength and subsurface fracture density.

[56] In the context of bedrock landslides, depth-dependent patterns of bedrock fracturing are predicted to strongly influence the typical depth of landslide failure. Landsliding occurs when the driving shear stresses become greater than the strength of the hillslope [Carson and Kirkby, 1972]. Bedrock fractures can reduce the rock mass strength below a localized critical value such that failure occurs. Additional controls on landslide failure include, but are not limited to, the hillslope angle, rainfall and pore pressures, and earthquake-induced ground accelerations [Keeper, 1984; Densmore and Hovius, 2000; Iverson, 2000; Meunier *et al.*, 2008].

[57] All other factors being equal, however, patterns of bedrock fracturing and the associated strength of the rock mass should modulate hillslope stability and failure depths. Bedrock that has been severely fractured by tectonic processes, such that the entire rock column maintains uniformly low rock mass strength, places no limits on the depth of landslides. In such cases, deep and/or frequent slides can remove any previously developed geomorphically fractured layer, as well as underlying swaths of tectonically fractured material (Figure 10). Such deep and/or frequent failures should uncover new surfaces underlain by bedrock with similarly uniform subsurface velocities and fracture densities determined by the pervasive tectonic fractures. In bedrock with minimal tectonic fracturing, in which bedrock at depth retains significant strength, landslide failure may not occur until geomorphic fracturing significantly reduces the rock mass strength. In such cases the depths of bedrock landslides would tend to be restricted to within the depth extent of the geomorphically fractured zone. If landsliding occurs at depths less than the full extent of this geomorphically fractured zone, the remaining depth profile would resemble a truncated version of the pre-failure profile (Figure 10). If instead, failure occurs at the base of the geomorphically fractured layer, the residual bedrock surface would be comprised solely of a single tectonically fractured layer.

[58] The above scenarios describe how subsurface patterns of bedrock fractures govern the potential depths of landslides and the residual fracture-density profiles immediately after failure. Because landslides are episodic events, commonly with long recurrence intervals, fracture profiles continue to develop between successive events. The extent of this development, however, is dependent on the time interval between landslides and the rate of surface-down geomorphic fracturing (Figure 10). Long recurrence intervals and rapid geomorphic fracturing produce deeper and more densely fractured profiles.

[59] The magnitude-frequency statistics of landslides from the Southern Alps and Fiordland (Figure 2) reveal striking differences in their average temporal and spatial impact (Table 3). Based on the power law fit to the landslide distributions, on average in the Southern Alps, a landslide $>100 \text{ m}^2$ should affect every part of the landscape approximately every 150 years. Landslides with depths of $<1.5 \text{ m}$ are predicted about every 300 years, whereas landslides with depths exceeding 5 m are predicted about every 750 years. In stark contrast, the entire landscape in Fiordland is predicted to experience a landslide $>100 \text{ m}^2$ once every 6 ky, landslides $<1.5 \text{ m}$ thick should occur at every location

Table 3. Landslide Magnitude-Frequency Statistics

Location	Number of Landslides	Average Landslide-Derived Erosion Rate (mm/yr)	<1.5 m		1.5–5 m		<5 m		5–15 m		<15 m		15–50 m		>50 m	
			Percent Coverage per ky ^a	Time For Total Coverage (yrs) ^b	Percent Coverage per ky	Time For Total Coverage (yrs)	Percent Coverage per ky	Time For Total Coverage (yrs)	Percent Coverage per ky	Time For Total Coverage (yrs)	Percent Coverage per ky	Time For Total Coverage (yrs)	Percent Coverage per ky	Time For Total Coverage (yrs)	Percent Coverage per ky	Time For Total Coverage (yrs)
Southern Alps	7,691	9 ± 4	300	333	205	487	505	198	133	753	638	157	99	1,012	737	136
Fiordland	2,211	0.1 ± 0.05 to 0.3 ± 0.1	7	15,308	6	17,866	12	8,286	4	22,717	16	6,139	No Observations	No Observations	No Observations	No Observations

^a“Percent Coverage per ky” refers to the percentage of the landscape predicted to be affected by landslides of a given depth (size) per thousand years.

^b“Time for Total Coverage” refers to the predicted time, in years, for landslides of a given depth (size) to affect the entire landscape. Both Percent Coverage per ky and Time for Total Coverage are calculated from the best power-law fit to the landslide magnitude-frequency distributions (Figure 2).

across the landscape every ~15 ky and landslides with depths exceeding 5 m are only expected over the full extent of the landscape once every ~23 ky.

[60] These estimates for landslide frequency and depth provide an illuminating context for interpreting the velocity and apparent fracture-density profiles from each study site. Whereas we predict that the rate of downward geomorphic fracturing is faster in the Southern Alps than in Fiordland, due to the intrinsically weaker rocks in the former, the frequency of landsliding is also far greater (Figure 2 and Table 3). The dominance of single-layer profiles in the Southern Alps (74%) is consistent with frequent failures to depths within the domain of tectonic fracturing, whereas less frequent landsliding in Fiordland allows sufficient time for the vast majority (67%) of sites to develop thick, geomorphically fractured profiles (Figures 9 and 10 and Table 3). On the other hand, counter to our expectations based on landslide frequencies, one-quarter of the Southern Alps profiles include a geomorphically fractured upper layer, whereas one-third of the Fiordland profiles reveal a single layer of uniformly fractured rock (Figure 9). In the Southern Alps, the preservation of near-surface geomorphic fracturing suggests that some parts of the landscape have not experienced deep failures over time periods long enough for geomorphic processes to produce strong, subsurface fracture gradients. In Fiordland, the uniformly fractured profiles are interpreted to result both from a tendency of some highly tectonically fractured rocks to fail more frequently, irrespective of the presence of a geomorphically weakened layer, and from the likelihood that more frequent, shallow landslides may have removed the geomorphically influenced layer. Moreover, the distribution and range of upper-layer, apparent fracture-density profiles (Figures 9c and 9d) suggest that they capture diverse stages of both geomorphic fracture propagation and truncation of previously thicker profiles.

[61] The normalized apparent fracture-density profiles (Figures 9a and 9b) reveal a key threshold within each region that predicts whether or not an upper, geomorphically fractured layer can be developed and maintained. In the Southern Alps, profiles with apparent fracture densities greater than ~10% in the lower layer are (with one exception) represented by single layers with uniformly fractured bedrock (Figure 9a). Conversely, all but one of the multi-layer profiles overlie lower-layer bedrock with apparent fracture densities less than ~10%. A similar pattern emerges in Fiordland, but the threshold occurs at a higher apparent fracture density of ~20%: twice as great as in the Southern Alps. In Fiordland, all but one (96%) of the profiles with a lower-layer, apparent fracture density greater than ~20% reveals a single, uniformly fractured subsurface layer, whereas lower-layer apparent fracture densities less than ~20% are overwhelmingly associated with multilayer profiles that display strong fracture gradients in the upper layer (Figure 9b).

[62] We interpret these thresholds, which discriminate between the presence or absence of multilayer profiles, not as boundaries related to precise fracture densities, but rather as boundaries separating domains that exhibit different geomorphic behavior with respect to landsliding. We infer that the uniformly fractured, single-layer profiles with apparent fracture densities greater than these threshold

values (~10% in the Southern Alps and ~20% in Fiordland) represent bedrock that has been sufficiently fractured by tectonic processes, such that frequent bedrock landslides (deep or shallow) or persistent rockfall/scree production effectively remove any geomorphic fracturing. Such deep or frequent failures leave apparent fracture-density profiles in the underlying rock that are characterized solely by spatially uniform, tectonic fracturing. The absence of geomorphic fracturing in these profiles also suggests that either landsliding has occurred relatively recently or that rates of geomorphic fracturing are sufficiently slow, such that no observable fracture gradient has developed since the last profile-clearing event.

[63] Surveys with lower-layer, apparent fracture densities less than the observed threshold value encompass both multilayer and single-layer profiles. In these cases, we interpret that tectonic fracturing at depth has been less extensive, such that these sites are less susceptible to the profile-clearing landslides that more readily occur in highly fractured rock. Although landslides still may occur, driven by earthquakes, excessive rainfall, or along discontinuities located deeper than resolvable with this shallow seismic technique, the lower density of tectonically induced fractures within these sites suggests that they are intrinsically more stable and, therefore, likely to fail only after geomorphic fracturing has further reduced the rock mass strength. If these sites are indeed less susceptible to landsliding, they should also have longer residence times at the surface and, thus, be more prone to developing geomorphic fracture gradients within the shallow subsurface (Figures 9 and 10). As geomorphic fracturing reduces the rock mass strength within this near-surface layer, however, the potential increases for hillslope failure to occur at depths equal to or shallower than the depth-extent of geomorphic fracturing. Given the contrasts in presumed intact strength between the granites and gneisses of Fiordland and the low-to-medium grade schists and greywacke/argillite of the Southern Alps [Augustinus, 1992a], it is not surprising that we observe a twofold (10% versus 20%) difference in the average, apparent fracture-density thresholds between these regions. The exact fracture density that results in unstable hillslopes at any given site, however, is expected to vary widely and be dependent on the local intact rock strength and all other influential local factors. Therefore, the apparent fracture-density thresholds identified for these regions should be considered as general, regional estimates based on the average conditions of each range.

[64] In Fiordland, the slow pace of surface erosion by bedrock landsliding, estimated to be between ~0.1 and ~0.3 mm/yr [Clarke and Burbank, 2010], allows geomorphic processes to develop deep subsurface fracture profiles across a majority of the landscape. This focused strength reduction of otherwise stable bedrock largely limits the depth of bedrock landslides to within the geomorphically fractured layer. This proposed link between bedrock fracturing and landslide processes is supported by the distribution of landslide depths (Figure 2) and patterns of bedrock fracturing (Figures 7b, 9b, and 9d). In Fiordland, three-quarters of the multilayer seismic surveys have geomorphically fractured upper layers between 2 and 10 m thick (Figure 6c): the same depths that account for most of the erosion by bedrock landslides (Figure 2). Although land-

slides <2 m thick occur more frequently, their volumetric contribution to landslide-driven erosion is far less significant [Hovius *et al.*, 1997; Clarke and Burbank, 2010] and such shallow slides would only impact the uppermost part of the fracture profiles. Similarly, the largest observed landslides in our Fiordland database have estimated depths of ~15 m: equivalent to the deepest measured geomorphically fractured upper-layer (Figures 6c and 9d). Overall in Fiordland, strong bedrock at depth and slow rates of landslide-driven erosion allow for development of deep, dense fracture gradients in the upper few meters of bedrock (Figures 7, 9, and 10). Only after the intrinsic rock strength is sufficiently reduced by geomorphic fracturing are bedrock landslides triggered within this highly fractured upper layer.

[65] In the Southern Alps, landslide-driven erosion reaches rates of ~9 mm/yr [Hovius *et al.*, 1997]. Therefore, although the same geomorphic fracturing processes that leave such a strong signature in Fiordland are undoubtedly active in the Southern Alps, the rapid rate of surface removal by bedrock landslides only allows geomorphic fracture gradients to develop at locations that are less susceptible to landsliding and/or are underlain by less fractured bedrock. Although the deepest seismically determined upper-layer depth extends to ~12 m, three-quarters of all Southern Alps sites display uniform fracture densities indicative of ubiquitous tectonic fracturing. Comparison of apparent fracture-density profiles with landslide distributions (Figures 2 and 9) reveals that uniform fracturing within the Southern Alps bedrock appears sufficient to reduce the rock mass strength such that landslide failure can occur at depths of up to ~50 m (Figure 2). Overall, in the Southern Alps, intrinsically weak rock that has been tectonically fractured to the verge of instability has made the region susceptible to bedrock landslides over a wide range of depths that appear largely independent of the extent of geomorphic fracturing.

[66] Comparison of the landslide distributions from the Southern Alps and Fiordland reveal order-of-magnitude differences in both the frequency of landsliding events and the largest observed landslides within each region (Figure 2). The Southern Alps and Fiordland are both characterized as threshold landscapes, in which the rate of landslide-driven erosion balances the rate of rock uplift [Hovius *et al.*, 1997; Clarke and Burbank, 2010]. Therefore, the differences in both the frequency of landsliding and the resulting rates of landslide-driven erosion (Figure 2 and Table 3) are not surprising given the order-of-magnitude contrast in rock uplift rates. There is no a priori reason, however, to expect differences in the largest landslide events given that hillslope lengths and local relief are similar between field sites [Clarke and Burbank, 2010]. Our seismic-survey results provide a potential explanation whereby the order-of-magnitude difference in the largest observed landslides (Figure 2) result from fundamental differences in the subsurface patterns of bedrock fracturing (Figure 9). The depth of near-surface, geomorphic fracturing in Fiordland limits the maximum depth and size of bedrock landslides, which results in a landslide distribution with a truncated large-magnitude tail (Figure 2). Conversely, pervasive tectonic fracturing in the Southern Alps allows large, deep landslides limited only by hillslope lengths and relief. Therefore, the presence or absence of large-magnitude landslides (depths > 15 m) appears to be a geomorphic consequence of the

contrasting subsurface strengths engendered by the different fracturing regimes.

[67] Although we primarily focus on examining the role of fractures in influencing hillslope stability and the depth of bedrock landslides, the seismic approach presented here may have potential for quantifying bedrock erodibility and assessing the erosional efficiency of other surface processes. Bedrock fractures may greatly reduce rock mass strength by partially or fully disintegrating rock fragments and, therefore, reduce resistance to physical erosion. Furthermore, bedrock fractures increase the surface area and hydraulic connectivity within a rock mass, thereby increasing the effectiveness of chemical weathering and solution processes which in turn may further reduce rock mass strength, increase erosional efficiency, and provide a potential mechanistic linkage between rates of physical and chemical erosion [Jacobson and Blum, 2003; Anderson *et al.*, 2007; Hren *et al.*, 2007; Willenbring and von Blanckenburg, 2010]. Bedrock fractures and fracturing mechanisms play a vital, yet poorly understood role in the “critical zone” by helping transform intact rock into sediment-mantled slopes [Anderson *et al.*, 2007]. Further development of this new seismically based field method for quantifying subsurface velocity structures and depth-dependent patterns of bedrock fractures may lead to a better understanding of the interactions between bedrock substrate and both chemical and physical erosional processes.

5. Conclusion

[68] We present a new method for assessing bedrock fractures in the shallow subsurface based on seismic refraction surveys. Two simple numerical models allow us to invert field and laboratory seismic surveys in order to obtain velocity and apparent fracture-density depth profiles. We compare model results from large populations of surveys collected in the relatively slowly eroding mountains of Fiordland and in the rapidly eroding Southern Alps of New Zealand. Our analysis reveals two end-member scenarios: bedrock that is uniformly fractured with depth; and bedrock in which a uniformly fractured layer is overlain by a layer containing a strong fracture gradient. Based on these fracture patterns, we argue that bedrock fracturing is governed by either tectonic or geomorphic mechanisms, which each produce their own fracture signature within the rock column. Tectonic processes generate uniform and pervasive fracture patterns that result in similarly uniform seismic velocity and fracture-density depth profiles. Conversely, geomorphic processes produce dense fracturing at the surface that decreases with depth, such that strong, depth-dependent gradients develop in both the velocity and fracture-density profiles. These geomorphically induced fracture gradients appear restricted to the shallow subsurface (usually <10 m depth) and overlie uniformly fractured bedrock at depth.

[69] We argue that rock mass strength is dependent on both the strength of intact rock and the density of fractures that reduce that strength. We suggest that the similar threshold slope angles in Fiordland and the Southern Alps result from similar hillslope-scale surface strengths, despite the differences in the underlying rock types. In Fiordland, a vast majority of the surveys reveal strong intact rock that has been geomorphically fractured with average apparent frac-

ture densities of ~40% at the surface. In contrast, the Southern Alps are dominated by uniform, tectonically fractured rock with average apparent fracture densities at the surface of ~10%. Therefore, we argue that the dense surface fracturing of the intrinsically strong rock of Fiordland results in an equivalent surface strength to the less densely fractured, but intrinsically weaker rock of the Southern Alps.

[70] At subsurface depths, the strength and stability of the rock mass are governed by the balance between the intact rock strength and the depth-dependent density of bedrock fractures. Based on the distributions of apparent fracture-density profiles, we identify regional fracture-density thresholds that separate relatively stable from unstable bedrock. When tectonically induced, apparent fracture densities exceed ~10% in the Southern Alps and ~20% in Fiordland, bedrock is, on average, sufficiently unstable such that slopes are susceptible to deep and/or frequent landslides, which preclude geomorphic development of near-surface fracture gradients. Conversely, when fracture densities are less than these threshold values, bedrock slopes remain relatively stable until geomorphic fracturing further reduces the hillslope-scale rock mass strength to the point that the slope is susceptible to bedrock landslides.

[71] In the Southern Alps, the landscape is dominated by bedrock that is uniformly fractured with depth and has an average apparent fracture density of ~10%: equivalent to the regional instability threshold. The predominance of bedrock that has been tectonically fractured to the verge of instability results in generally unstable hillslopes capable of producing large landslides with depths far greater than the extent of geomorphic fracturing. Conversely, the Fiordland subsurface is largely characterized by multilayer profiles with an average apparent fracture density of only 5% in the deep subsurface, far less than the regional instability threshold of ~20%. The generally stable bedrock and slower rates of erosion allow geomorphic processes to develop strong fracture gradients within the shallow subsurface. Only after the rock mass strength has been reduced by geomorphic fracturing do hillslopes become unstable. Therefore, the depths of bedrock landslides in Fiordland are generally limited to within this geomorphically fractured zone.

[72] Overall, this new seismic refraction-based methodology appears capable of quantifying bedrock-fracture patterns at hillslope scales. We infer that depth-dependant patterns of subsurface fractures play a prominent role in influencing surface form and erosive processes. Although rates of landslide-driven erosion in both Fiordland and the Southern Alps are responding to rates of tectonic uplift and valley incision, we suggest that the density and depth of bedrock fractures modulates the magnitude and frequency of landslides required to achieve these rates.

Notation

V_{avg}	average upper layer velocity	km/s
V_m	lower layer velocity	km/s
V_o	initial surface velocity	km/s
V_c	velocity at the base of the lower layer	km/s
V	modeled subsurface velocity	km/s
h	thickness of upper layer	m
t_o	time intercept	ms
t	time	ms

x	distance	m
a	velocity gradients	km/s/m
z	depth	m
l	unit length	m
l_f	unit length of fracture space	m
l_r	unit length of intact rock	m
t_f	time for seismic wave to travel through the unit length of fracture space	ms
t_r	time for seismic wave to travel through the unit length of intact rock	ms
P_f	fraction of fracture space	—
P_r	fraction of rock	—
V_f	velocity of fracture space	km/s
V_r	velocity of intact rock	km/s

[73] **Acknowledgments.** We thank Jordan Lewis and Colin Amos for assistance collecting field seismic surveys, as well as Fiordland Ecology Holidays, Fiordland Helicopters, the University of Canterbury, and the Fiordland DOC office for field and logistical support. We are grateful to Gary Mavko and the Stanford Rock Physics group for guidance and assistance with laboratory velocity measurement. Tom Dunne, Bodo Bookhagen, Tim Stern, and Ralph Archuleta provided valuable guidance and discussion. We appreciate the thorough and insightful reviews by D. Miller, T. C. Hales, and two anonymous reviewers, as well as constructive comments and suggestions from the editors, A. Densmore and M. Church, and from associate editor S. Mudd, all of which greatly improved this manuscript. This project was funded by the National Geographic Society, NSF (EAR 0117242), and the Petroleum Research Fund (41960-AC8).

References

- Anderson, R. S. (1998), Near-surface thermal profiles in alpine bedrock: Implications for the frost weathering of rock, *Arct. Alp. Res.*, 30(4), 362–372, doi:10.2307/1552008, doi:10.2307/1552008.
- Anderson, S. P., F. von Blanckenburg, and A. F. White (2007), Physical and chemical controls on the critical zone, *Elements*, 3(5), 315–319, doi:10.2113/gselements.3.5.315, doi:10.2113/gselements.3.5.315.
- Augustinus, P. C. (1992a), Outlet glacier trough size–drainage area relationships, Fiordland, New Zealand, *Geomorphology*, 4(5), 347–361, doi:10.1016/0169-555X(92)90028-M.
- Augustinus, P. C. (1992b), The influence of rock mass strength on glacial valley cross-profile morphometry: A case study from the Southern Alps, New Zealand, *Earth Surf. Processes Landforms*, 17(1), 39–51, doi:10.1002/esp.3290170104, doi:10.1002/esp.3290170104.
- Augustinus, P. C. (1995), Glacial valley cross-profile development: The influence of in situ rock stress and rock mass strength, with examples from the Southern Alps, New Zealand, *Geomorphology*, 14(2), 87–97, doi:10.1016/0169-555X(95)00050-X.
- Bansal, R., and M. K. Sen (2008), Finite-difference modelling of S-wave splitting in anisotropic media, *Geophys. Prospect.*, 56(3), 293–312, doi:10.1111/j.1365-2478.2007.00693.x.
- Beaumont, C., P. J. J. Kamp, J. Hamilton, and P. Fullsack (1996), The continental collision zone, South Island, New Zealand: Comparison of geodynamical models and observations, *J. Geophys. Res.*, 101(B2), 3333–3359, doi:10.1029/95JB02401, doi:10.1029/95JB02401.
- Berryman, J. G. (2007), Seismic waves in rocks with fluids and fractures, *Geophys. J. Int.*, 171(2), 954–974, doi:10.1111/j.1365-246X.2007.03563.x.
- Bieniawski, Z. T. (1989), *Engineering Rock Mass Classifications: A Complete Manual for Engineers and Geologists in Mining, Civil, and Petroleum Engineering*, John Wiley, New York.
- Boadu, F. K. (1997), Rock properties and seismic attenuation: Neural network analysis, *Pure Appl. Geophys.*, 149(3), 507–524, doi:10.1007/s000240050038, doi:10.1007/s000240050038.
- Boadu, F. K., and L. T. Long (1996), Effects of fractures on seismic-wave velocity and attenuation, *Geophys. J. Int.*, 127(1), 86–110, doi:10.1111/j.1365-246X.1996.tb01537.x.
- Bradshaw, J. Y. (1990), Geology of crystalline rocks of northern Fjordland – details of the granulite facies western Fjordland orthogneiss and associated rock units, *N.Z. J. Geol. Geophys.*, 33(3), 465–484.
- Brady, B. H. G., and E. T. Brown (2006), *Rock Mechanics: For Underground Mining*, 3rd ed., Springer, Dordrecht, The Netherlands.
- Brocher, T. M., and N. I. Christensen (1990), Seismic anisotropy due to preferred mineral orientation observed in shallow crustal rocks in Southern Alaska, *Geology*, 18(8), 737–740, doi:10.1130/0091-7613(1990)018<0737:SADTPM>2.3.CO;2.
- Budetta, P., R. de Riso, and C. De Luca (2001), Correlations between jointing and seismic velocities in highly fractured rock masses, *Bull. Eng. Geol. Environ.*, 60(3), 185–192, doi:10.1007/s100640100097.
- Burbank, D. W., J. Leland, E. Fielding, R. S. Anderson, N. Brozovic, M. R. Reid, and C. Duncan (1996), Bedrock incision, rock uplift and threshold hillslopes in the northwestern Himalayas, *Nature*, 379(6565), 505–510, doi:10.1038/379505a0, doi:10.1038/379505a0.
- Carson, M. A., and M. J. Kirkby (1972), *Hillslope Form and Process*, Cambridge Univ. Press, London.
- Cha, M., G. C. Cho, and J. C. Santamarina (2009), Long-wavelength P-wave and S-wave propagation in jointed rock masses, *Geophysics*, 74(5), E205–E214, doi:10.1190/1.3196240, doi:10.1190/1.3196240.
- Clarke, B. A., and D. W. Burbank (2010), Bedrock fracturing, threshold hillslopes, and limits to the magnitude of bedrock landslides, *Earth Planet. Sci. Lett.*, 297(3–4), 577–586, doi:10.1016/j.epsl.2010.07.011.
- Cosgrove, J. W. (1998), The role of structural geology in reservoir characterization, in *Structural Geology in Reservoir Characterization*, *Geol. Soc. Spec. Publ.*, 127, edited by M. P. Coward, T. S. Daltaban, and H. Johnson, pp. 1–13, The Geol. Soc., London.
- Coulomb, C. A. (1776), Essais sur une application des règles de maximis et minimis à quelques problèmes de statique, relatifs à l'architecture, *Mém. Mathématique Physique*, 7(343), 343–382.
- Crampin, S., and J. H. Lovell (1991), A decade of shear-wave splitting in the Earth's crust: What does it mean? what use can we make of it? and what should we do next? *Geophys. J. Int.*, 107(3), 387–407, doi:10.1111/j.1365-246X.1991.tb01401.x.
- Deere, D. U. (1964), Technical descriptions of rock cores for engineering purposes, *Rock Mech. Rock Eng.*, 1, 107–116.
- DeMets, C., R. G. Gordon, D. F. Argus, and S. Stein (1990), Current plate motions, *Geophys. J. Int.*, 101(2), 425–478, doi:10.1111/j.1365-246X.1990.tb06579.x.
- Densmore, A. L., and N. Hovius (2000), Topographic fingerprints of bedrock landslides, *Geology*, 28(4), 371–374, doi:10.1130/0091-7613(2000)28<371:TFOBL>2.0.CO;2.
- Duvall, A., E. Kirby, and D. Burbank (2004), Tectonic and lithologic controls on bedrock channel profiles and processes in coastal California, *J. Geophys. Res.*, 109, F03002, doi:10.1029/2003JF000086.
- Eberhart-Phillips, D., and M. Reyners (2001), A complex, young subduction zone imaged by three-dimensional seismic velocity, Fiordland, New Zealand, *Geophys. J. Int.*, 146(3), 731–746, doi:10.1046/j.0956-540x.2001.01485.x.
- El-Naqa, A. (1996), Assessment of geomechanical characterization of a rock mass using a seismic geophysical technique, *Geotech. Geol. Eng.*, 14(4), 291–305, doi:10.1007/BF00421945.
- Forbriger, T. (2003a), Inversion of shallow-seismic wavefields: I. Wavefield transformation, *Geophys. J. Int.*, 153(3), 719–734, doi:10.1046/j.1365-246X.2003.01929.x.
- Forbriger, T. (2003b), Inversion of shallow-seismic wavefields: II. Inferring subsurface properties from wavefield transforms, *Geophys. J. Int.*, 153(3), 735–752, doi:10.1046/j.1365-246X.2003.01985.x.
- Fratta, D., and J. C. Santamarina (2002), Shear wave propagation in jointed rock: State of stress, *Geotechnique*, 52(7), 495–505, doi:10.1680/geot.2002.52.7.495, doi:10.1680/geot.2002.52.7.495.
- Gabet, E. J., and S. M. Mudd (2010), Bedrock erosion by root fracture and tree throw: A coupled biogeomorphic model to explore the humped soil production function and the persistence of hillslope soils, *J. Geophys. Res.*, 115, F04005, doi:10.1029/2009JF001526.
- Gilbert, G. K. (1877), Land sculpture, in *Report on the Geology of the Rocky Mountains: Geographical and Geological Survey of the Rocky Mountain Region*, edited by G. K. Gilbert and C. E. Dutton, pp. 99–150, U.S. Gov. Print. Office, Washington, D. C.
- Griffiths, G. A., and M. J. McSaveney (1983), Distribution of mean annual precipitation across some steepland regions of New Zealand, *N. Z. J. Sci.*, 26(2), 197–209.
- Hack, R. (2000), Geophysics for slope stability, *Surv. Geophys.*, 21(4), 423–448, doi:10.1023/A:1006797126800.
- Hales, T. C., and J. J. Roering (2005), Climate-controlled variations in scree production, Southern Alps, New Zealand, *Geology*, 33(9), 701–704, doi:10.1130/G21528.1.
- Hales, T. C., and J. J. Roering (2007), Climatic controls on frost cracking and implications for the evolution of bedrock landscapes, *J. Geophys. Res.*, 112, F02033, doi:10.1029/2006JF000616.
- Hales, T. C., and J. J. Roering (2009), A frost “buzzsaw” mechanism for erosion of the eastern Southern Alps, New Zealand, *Geomorphology*, 107(3–4), 241–253, doi:10.1016/j.geomorph.2008.12.012.
- Heincke, B., H. Maurer, A. G. Green, H. Willenberg, T. Spillmann, and L. Burlini (2006), Characterizing an unstable mountain slope using

- shallow 2D and 3D seismic tomography, *Geophysics*, 71(6), B241–B256, doi:10.1190/1.2338823.
- Herman, F., and J. Braun (2006), Fluvial response to horizontal shortening and glaciations: A study in the Southern Alps of New Zealand, *J. Geophys. Res.*, 111, F01008, doi:10.1029/2004JF000248.
- Herman, F., J. Braun, and W. J. Dunlap (2007), Tectonomorphic scenarios in the Southern Alps of New Zealand, *J. Geophys. Res.*, 112, B04201, doi:10.1029/2004JB003472.
- Herman, F., S. C. Cox, and P. J. J. Kamp (2009), Low-temperature thermochronology and thermokinematic modeling of deformation, exhumation, and development of topography in the central Southern Alps, New Zealand, *Tectonics*, 28(5), TC5011, doi:10.1029/2008TC002367.
- Hoek, E., and J. W. Bray (1997), *Rock Slope Engineering*, 3rd ed., Inst. of Min. and Metal, London.
- Hoek, E., and E. T. Brown (1997), Practical estimates of rock mass strength, *Int. J. Mech. Min. Sci. Geomech. Abstr.*, 34(8), 1165–1186, doi:10.1016/S1365-1609(97)80069-X.
- House, M. A., M. Gurnis, P. J. J. Kamp, and R. Sutherland (2002), Uplift in the Fiordland region, New Zealand: Implications for incipient subduction, *Science*, 297(5589), 2038–2041, doi:10.1126/science.1075328.
- House, M. A., M. Gurnis, R. Sutherland, and P. J. J. Kamp (2005), Patterns of Late Cenozoic exhumation deduced from apatite and zircon U–He ages from Fiordland, New Zealand, *Geochem. Geophys. Geosyst.*, 6, Q09013, doi:10.1029/2005GC000968.
- Hovius, N., C. P. Stark, and P. A. Allen (1997), Sediment flux from a mountain belt derived by landslide mapping, *Geology*, 25(3), 231–234, doi:10.1130/0091-7613(1997)025<0231:SFFAMB>2.3.CO;2.
- Hren, M. T., C. P. Chamberlain, G. E. Hilley, P. M. Blisniuk, and B. Bookhagen (2007), Major ion chemistry of the Yarlung Tsangpo–Brahmaputra river: Chemical weathering, erosion, and CO₂ consumption in the southern Tibetan plateau and eastern syntaxis of the Himalaya, *Geochim. Cosmochim. Acta*, 71(12), 2907–2935, doi:10.1016/j.gca.2007.03.021.
- Hudson, J. A. (1980), Overall properties of a cracked solid, *Math. Proc. Cambridge Philos. Soc.*, 88(2), 371–384, doi:10.1017/S0305004100057674.
- Hudson, J. A. (1981), Wave speeds and attenuation of elastic waves in material containing cracks, *Geophys. J. R. Astron. Soc.*, 64(1), 133–150, doi:10.1111/j.1365-246X.1981.tb02662.x.
- Iverson, R. M. (2000), Landslide triggering by rain infiltration, *Water Resour. Res.*, 36(7), 1897–1910, doi:10.1029/2000WR900090.
- Jacobson, A. D., and J. D. Blum (2003), Relationship between mechanical erosion and atmospheric CO₂ consumption in the New Zealand Southern Alps, *Geology*, 31(10), 865–868, doi:10.1130/G19662.1.
- Jaeger, J. C., N. G. W. Cook, and R. W. Zimmerman (2007), *Fundamentals of Rock Mechanics*, 4th ed., Blackwell, Malden, Mass.
- Kahraman, S. (2001), A correlation between P-wave velocity, number of joints and Schmidt hammer rebound number, *Int. J. Rock Mech. Min. Sci.*, 38(5), 729–733, doi:10.1016/S1365-1609(01)00034-X.
- Kamp, P. J. J., and J. M. Tippet (1993), Dynamics of Pacific plate crust in the South Island (New Zealand) zone of oblique continent–continent convergence, *J. Geophys. Res.*, 98(B9), 16,105–16,118, doi:10.1029/93JB01091.
- Keeper, D. K. (1984), Landslides caused by earthquakes, *Geol. Soc. Am. Bull.*, 95(4)406421, doi:10.1130/0016-7606(1984)95<406:LCBE>2.0.CO;2.
- Keiswetter, D. A., and D. W. Steeples (1995), A field investigation of source parameters for the sledgehammer, *Geophysics*, 60(4), 1051–1057, doi:10.1190/1.1443833.
- Koons, P. O. (1989), The topographic evolution of collisional mountain belts: A numerical look at the Southern Alps, New Zealand, *Am. J. Sci.*, 289, 1041–1069, doi:10.2475/ajs.289.9.1041.
- Koons, P. O. (1990), Two-sided orogen: Collision and erosion from the sandbox to the Southern Alps, New Zealand, *Geology*, 18(8), 679–682, doi:10.1130/0091-7613(1990)018<0679:TSCAE>2.3.CO;2.
- Korup, O. (2005), Geomorphic imprint of landslides on alpine river systems, southwest New Zealand, *Earth Surf. Processes Landforms*, 30(7), 783–800, doi:10.1002/esp.1171.
- Korup, O. (2008), Rock type leaves topographic signature in landslide-dominated mountain ranges, *Geophys. Res. Lett.*, 35, L11402, doi:10.1029/2008GL034157.
- Korup, O., and F. Schlunegger (2009), Rock-type control on erosion-induced uplift, eastern Swiss Alps, *Earth Planet. Sci. Lett.*, 278(3–4), 278–285, doi:10.1016/j.epsl.2008.12.012.
- Larsen, I. J., D. R. Montgomery, and O. Korup (2010), Landslide erosion controlled by hillslope material, *Nat. Geosci.*, 3(4), 247–251, doi:10.1038/ngeo776.
- Lavé, J., and D. Burbank (2004), Denudation processes and rates in the Transverse Ranges, southern California: Erosional response of a transitional landscape to external and anthropogenic forcing, *J. Geophys. Res.*, 109, F01006, doi:10.1029/2003JF000023.
- Leucci, G., and L. De Giorgi (2006), Experimental studies on the effects of fracture on the P and S wave velocity propagation in sedimentary rock (“Calcarene del Salento”), *Eng. Geol. Amsterdam*, 84(3–4), 130–142, doi:10.1016/j.enggeo.2005.12.004.
- Lin, G. W., H. Chen, N. Hovius, M. J. Horng, S. Dadson, P. Meunier, and M. Lines (2008), Effects of earthquake and cyclone sequencing on landslide and fluvial sediment transfer in a mountain catchment, *Earth Surf. Processes Landforms*, 33(9), 1354–1373, doi:10.1002/esp.1716.
- Liu, E. R., J. A. Hudson, and T. Pointer (2000), Equivalent medium representation of fractured rock, *J. Geophys. Res.*, 105(B2), 2981–3000, doi:10.1029/1999JB900306.
- Malservisi, R., K. P. Furlong, and H. Anderson (2003), Dynamic uplift in a transpressional regime: Numerical model of the subduction area of Fiordland, New Zealand, *Earth Planet. Sci. Lett.*, 206(3–4), 349–364, doi:10.1016/S0012-821X(02)01100-7.
- Martel, S. J. (2006), Effect of topographic curvature on near-surface stresses and application to sheeting joints, *Geophys. Res. Lett.*, 33, L01308, doi:10.1029/2005GL024710.
- Mason, B. (1962), Metamorphism in the Southern Alps of New Zealand, *Bull. Am. Mus. Nat. Hist.*, 123, 217–248.
- Meunier, P., N. Hovius, and J. A. Haines (2008), Topographic site effects and the location of earthquake induced landslides, *Earth Planet. Sci. Lett.*, 275(3–4), 221–232, doi:10.1016/j.epsl.2008.07.020.
- Miller, D. J., and T. Dunne (1996), Topographic perturbations of regional stresses and consequent bedrock fracturing, *J. Geophys. Res.*, 101(B11), 25,523–25,536, doi:10.1029/96JB02531.
- Molnar, P., R. S. Anderson, and S. P. Anderson (2007), Tectonics, fracturing of rock, and erosion, *J. Geophys. Res.*, 112, F03014, doi:10.1029/2005JF000433.
- Montgomery, D. R. (2001), Slope distributions, threshold hillslopes, and steady-state topography, *Am. J. Sci.*, 301(4–5), 432–454, doi:10.2475/ajs.301.4-5.432.
- Moon, B. P., and M. J. Selby (1983), Rock mass strength and scarp forms in southern Africa, *Geogr. Ann., Ser. A*, 65(1/2), 135–145, doi:10.2307/520727.
- Moore, J. R., J. W. Sanders, W. E. Dietrich, and S. D. Glaser (2009), Influence of rock mass strength on the erosion rate of alpine cliffs, *Earth Surf. Processes Landforms*, 34, 1339–1352, doi:10.1002/esp.1821.
- Mussett, A. E., and M. A. Khan (2000), *Looking Into the Earth: An Introduction to Geological Geophysics*, Cambridge Univ. Press, Cambridge, U. K.
- National Institute of Water and Atmospheric Research (2000), Mean annual precipitation data (1971–2000), <http://www.niwa.co.nz>.
- Ohmori, H. (1992), Morphological characteristics of the scar created by large-scale rapid mass movement, *Trans. Jap. Geomorph. Union*, 13, 185–202.
- Ohmori, H., and M. Hirano (1988), Magnitude, frequency and geomorphological significance of rocky mud flow, landcreep and the collapse of steep slopes, *Z. Geomorphol.*, 67, S55–S65.
- Okaya, D., N. Christensen, D. Stanley, and T. Stern (1995), Crustal anisotropy in the vicinity of the Alpine Fault Zone, South Island, New Zealand, *N.Z. J. Geol. Geophys.*, 38(4), 579–583, doi:10.1080/00288306.1995.9514686.
- Palmer, D. (1981), An introduction to the generalized reciprocal method of seismic refraction interpretation, *Geophysics*, 46(11), 1508–1518, doi:10.1190/1.1441157.
- Pyrak-Nolte, L. J., L. R. Myer, and N. G. W. Cook (1990a), Transmission of seismic-waves across single natural fractures, *J. Geophys. Res.*, 95(B6), 8617–8638, doi:10.1029/JB095iB06p08617.
- Pyrak-Nolte, L. J., L. R. Myer, and N. G. W. Cook (1990b), Anisotropy in seismic velocities and amplitudes from multiple parallel fractures, *J. Geophys. Res.*, 95(B7), 11,345–11,358, doi:10.1029/JB095iB07p11345.
- Rahn, P. H. (1996), *Engineering Geology: An Environmental Approach*, 2nd ed., Prentice-Hall, Upper Saddle River, N. J.
- Renalier, F., D. Jongmans, M. Campillo, and P.-Y. Bard (2010), Shear wave velocity imaging of the Avignonet landslide (France) using ambient noise cross correlation, *J. Geophys. Res.*, 115, F03032, doi:10.1029/2009JF001538.
- Schmidt, K. M., and D. R. Montgomery (1995), Limits to relief, *Science*, 270(5236), 617–620, doi:10.1126/science.270.5236.617.
- Schoenberg, M., and C. M. Sayers (1995), Seismic anisotropy of fractured rock, *Geophysics*, 60(1), 204–211, doi:10.1190/1.1443748.
- Selby, M. J. (1980), A rock mass strength classification for geomorphic purposes: With tests from Antarctica and New Zealand, *Z. Geomorphol.*, 24, 31–51.
- Selby, M. J. (1992), *Hillslope Materials and Processes*, 2nd ed., Oxford Univ. Press, Oxford, U. K.

- Sheriff, R. E., and L. P. Geldart (1982), *Exploration Seismology*, Cambridge Univ. Press, New York.
- Sjogren, B., A. Ofsthus, and J. Sandberg (1979), Seismic classification of rock mass qualities, *Geophys. Prospect.*, 27(2), 409–442, doi:10.1111/j.1365-2478.1979.tb00977.x.
- Stern, T., S. Kleffmann, D. Okaya, M. Scherwath, and S. Bannister (2001), Low seismic-wave speeds and enhanced fluid pressure beneath the Southern Alps of New Zealand, *Geology*, 29(8), 679–682, doi:10.1130/0091-7613(2001)029<0679:LSWSAE>2.0.CO;2.
- Stock, J. D., and D. R. Montgomery (1999), Geologic constraints on bedrock river incision using the stream power law, *J. Geophys. Res.*, 104(B3), 4983–4993, doi:10.1029/98JB02139.
- Suggate, R. P. (1990), Late Pliocene and Quaternary glaciations of New Zealand, *Quat. Sci. Rev.*, 9(2–3), 175–197, doi:10.1016/0277-3791(90)90017-5.
- Sutherland, R., F. Davey, and J. Beavan (2000), Plate boundary deformation in South Island, New Zealand, is related to inherited lithospheric structure, *Earth Planet. Sci. Lett.*, 177(3–4), 141–151, doi:10.1016/S0012-821X(00)00043-1.
- Sutherland, R., M. Gurnis, P. J. J. Kamp, and M. A. House (2009), Regional exhumation history of brittle crust during subduction initiation, Fiordland, southwest New Zealand, and implications for thermochronologic sampling and analysis strategies, *Geosphere*, 5(5), 409–425, doi:10.1130/GES00225.1.
- Telford, W. M., L. P. Geldart, R. E. Sheriff, and D. A. Keys (1990), *Applied Geophysics*, 770 pp., Cambridge Univ. Press, Cambridge, U. K.
- Terzaghi, K. (1962), Stability of steep slopes on hard unweathered rock, *Géotechnique*, 12(4), 251–270, doi:10.1680/geot.1962.12.4.251.
- Tippett, J. M., and P. J. J. Kamp (1993), Fission track analysis of the Late Cenozoic vertical kinematics of continental Pacific crust, South Island, New Zealand, *J. Geophys. Res.*, 98(B9), 16,119–16,148, doi:10.1029/92JB02115.
- Vilhelm, J., V. Rudajev, R. Živor, T. Lokajiček, and Z. Pros (2010), Influence of crack distribution of rocks on P-wave velocity anisotropy—A laboratory and field scale study, *Geophys. Prospect.*, 58(6), 1099–1110, doi:10.1111/j.1365-2478.2010.00875.x.
- Walder, J., and B. Hallet (1985), A theoretical model of the fracture of rock during freezing, *Geol. Soc. Am. Bull.*, 96(3), 336–346, doi:10.1130/0016-7606(1985)96<336:ATMOTF>2.0.CO;2.
- White, J. E. (1983), *Underground Sound: Application of Seismic Waves*, Elsevier Sci., New York.
- Willenbring, J. K., and F. von Blanckenburg (2010), Long-term stability of global erosion rates and weathering during late-Cenozoic cooling, *Nature*, 465(7295), 211–214, doi:10.1038/nature09044.
- Zelt, C. A., and R. B. Smith (1992), Seismic traveltimes inversion for 2-D crustal velocity structure, *Geophys. J. Int.*, 108(1), 16–34, doi:10.1111/j.1365-246X.1992.tb00836.x.
- Zhang, Y., C. M. Sayers, and J. I. Adachi (2009), The use of effective medium theories for seismic wave propagation and fluid flow in fractured reservoirs under applied stress, *Geophys. J. Int.*, 177(1), 205–221, doi:10.1111/j.1365-246X.2008.04073.x.

D. W. Burbank, Department of Earth Science, University of California Santa Barbara, Mail Code 1100, 1140 Girvetz Hall, Santa Barbara, CA 93106-1100, USA. (burbank@eri.ucsb.edu)

B. A. Clarke, Institute for Earth and Environmental Science, Universität Potsdam, Karl-Liebknecht-Str. 24-25, D-14476 Potsdam-Golm, Germany. (clarke@geo.uni-potsdam.de)